IMPACT OF ELECTRICAL CONTACTING SCHEME ON PERFORMANCE OF InGaN/GaN SCHOTTKY SOLAR CELLS

Aditya Jain

Thesis submitted to the faculty of the Virginia Polytechnic Institute and State University in partial fulfillment of the requirements for the degree of

Master of Science

In

Electrical Engineering

Louis J. Guido

Guo-Quan Lu

Paul Plassmann

Mariusz K. Orlowski

August 14, 2014

Blacksburg, VA

Keywords: Transparent conductive layer, Schottky solar cell, Device characterization

IMPACT OF ELECTRICAL CONTACTING SCHEME ON PERFORMANCE OF InGaN/GaN SCHOTTKY SOLAR CELLS

Aditya Jain

ABSTRACT

Realization of low-resistance electrical contacts on both sides of a solar cell is essential for obtaining the best possible performance. A key component of a solar cell is a metal contact on the illuminated side of the cell which should efficiently collect carriers. These contacts can be formed using an opaque metal grid/finger pattern. The metal electrode may be used alone or in combination with a broad-area transparent conductive film. This work aims at investigating the impact of the electrical contacting scheme employed in InGaN/GaN Schottky barrier solar cells on their performance. InGaN is a III-V compound semiconductor and has a tunable direct band-gap (0.7 eV to 3.4 eV) which spans most of the solar spectrum; this fact, along with other beneficial material properties, motivates the study of InGaN photovoltaic devices. A number of groups have recently investigated InGaN-based homo-junction and hetero-junction p-i-n solar cells. However, very few groups have worked on InGaN Schottky solar cells. Compared to p-n junctions, Schottky barrier solar cells are cheaper to grow and fabricate; they are also expected to improve the spectral response because of near surface depletion regions in the shorter wavelength regions. In this particular work on InGaN based solar cells, a Schottky diode structure was used to avoid the issue of highly resistive p-type InGaN. In this study, platinum (Pt) is used to form a Schottky barrier with an InGaN/GaN absorber region. Electrical and optical properties of platinum films are investigated as a function of their thickness. InGaN/GaN Schottky solar cells with platinum as the transparent conductive film are reported and their performance is evaluated as a function of the metal thickness.

Dedicated to my family, who always believed in me,

For their love and support.

To those who have inspired and motivated me.

To those who find joy in the thrill of creative effort.

Acknowledgements

I am deeply grateful to my advisor, *Dr. Louis Guido,* for his academic guidance and keen support over the last two years. I appreciate the time and effort that he has put in to our discussions and meetings; going as far as making time on the weekends. I will always be thankful to him for giving me an opportunity to work with him. I have learned a lot from him during my time here, a lot of which goes beyond the research aspect. I am thankful to *Dr. G. Q Lu, Dr. Paul Plassmann* and *Dr. Marius Orlowski* for serving on my committee; and for providing valuable insights on various issues relating to my thesis. A special thanks to *Dr. Paul Plassmann* for guiding me in the right direction when I needed it the most.

I would like to thank other members of Dr. Guido's research group for their help and support which includes: *Kevin, Noah, David, Tim, Eric and Rachel*. In particular, I would like to thank *Kevin* who has been an excellent mentor and guide. Kevin's guidance was extremely helpful, especially in the beginning, when I was completely new to this field of research. I would also like to thank *Donald Leber* for his assistance in using the Micron cleanroom facilities. I would like to thank all my *teachers* who have greatly enriched my learning experience here at Virginia Tech. I would also like to thank my ECE academic advisor, *Ms. Mary Brewer* for always giving me valuable advice right from my time here as an undergraduate student. I am grateful to the *Graduate School* and *Cranwell International Center* for all their help and support. I would also like to thank all my *friends* for their support, who have made my time here, memorable.

I am deeply grateful to my entire family to whom I dedicate this thesis. My grandfather, *Late Ravish Chandra Jain* has been a source of great inspiration. I would like to thank my grandmother, *Kusum Jain* who has been extremely supportive and motivating. I would like to thank my mother, *Sandhya Jain* who has been a constant source of encouragement and love. I would like to thank my father, *Anuj Jain* for his relentless support and faith in my abilities. Heartfelt thanks to my sister, *Vasudha Jain*, her husband, *Gaurav Jain* and their daughter, *Devina Jain* for their continued love and support. I would also like to thank my relatives and extended family here in the US who have been very supportive and helpful as well.

Although this thesis represents the work I did for my masters degree, it cannot express the long hours spent in lab, the joy of learning new things, the hope for good results and the sadness followed by each failed attempt. However, each attempt presented an opportunity to learn something new and it helped me appreciate the subject matter even more. Lastly, I would like to thank *Virginia Tech* for providing a congenial and supportive environment for learning; and for the memories that I will cherish forever.

Table of Contents

List of Figures

List of Tables

Chapter 1. Introduction

1.1 Harnessing the power of the sun

According to the International Energy Outlook 2013 report, world energy consumption will increase by 56 percent between 2010 and 2040 [1]. Total world energy use will rise from 524 quadrillion British thermal units (Btu) in 2010 to 820 quadrillion Btu in 2040, as shown in *Figure 1.1* [1]. At present, we are dependent on non-renewable sources of energy like coal, petroleum and natural gas for most of our energy needs. However, use of these conventional energy sources is believed to be the root cause of global warming and thus, climate change. Climate change is one of the biggest environmental challenges that the world is facing today. The need of the hour is to consider ways of reducing our carbon footprint by sourcing our energy needs from renewable energy sources. Global atmospheric concentrations of greenhouse gases which are responsible for global warming have increased alarmingly in the past few years. The Keeling curve shown in *Figure 1.2* is an indication of the man-made increases of greenhouse gases (specifically carbon-dioxide) that contribute towards global warming [2]. Our dependence on non-renewable sources of energy has increased so much that it also poses the question of how well we would cope in their absence. Hence, this is the correct time to start looking for alternative energy sources. While we look for alternative solutions, one of them can be found directly above us, the Sun!

Solar illumination offers a clean and inexhaustible source of energy. Electric power can be harnessed from the sun either through thermal or photovoltaic means.

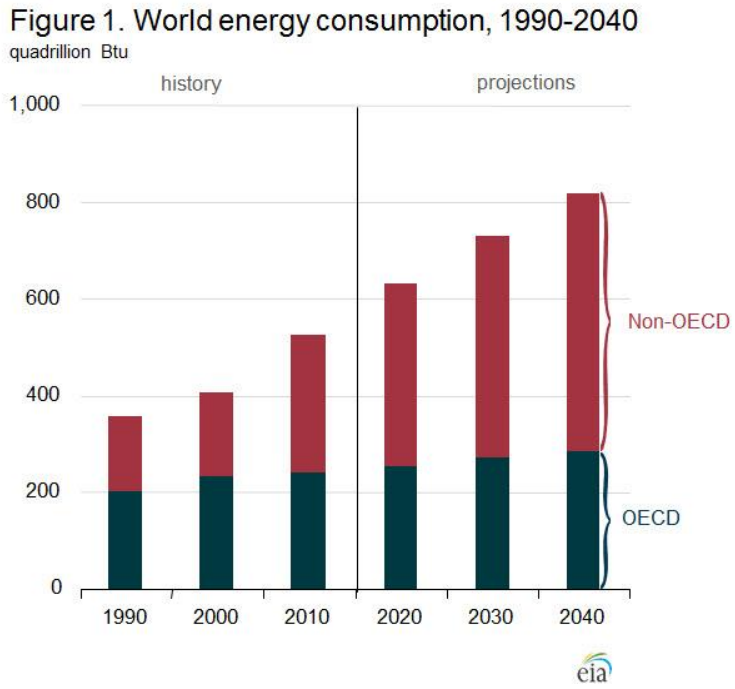

Figure 1.1 World Energy Consumption (1990-2040), U. S. E. I. Administration, "International Energy Outlook 2013," ed, 2013. Used under fair use, 2014.

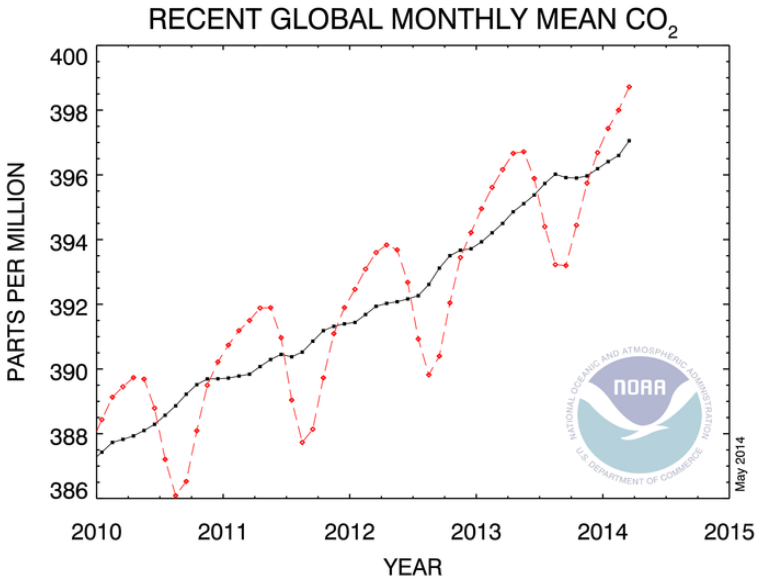

Figure 1.2 Recent Trend in Global Carbon Dioxide Concentrations, N. O. A. Administration, "Trends in Atmospheric Carbon Dioxide," ed, 2014. Used under fair use, 2014.

Solar energy has by far the highest potential of all the renewable sources of energy. The sun provides an average of 89,000 terawatts to the earth's surface. The black dots shown in *Figure 1.3* represent locations that could provide for more than the world's electricity demand, if dedicated to solar energy harvesting [3]. Therefore, efficient systems that harness the sun's energy must be designed and implemented. Solar cells convert the sun's light directly into electricity via the photovoltaic effect. The setup is easy to install; and the process is highly reliable with low operation and low maintenance costs. It can be a stand-alone system or it could be integrated with storage systems or connected to the grid. More importantly, this process is environmental friendly. Therefore, development of highly efficient, low cost solar cells is an important topic that needs to be studied.

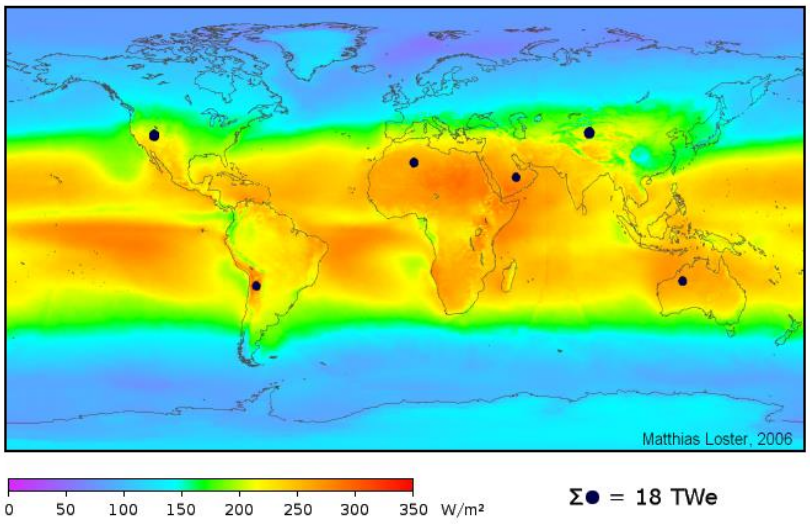

Figure 1.3 Black dots could provide more than the world's total energy demand, M. Loster, "Total Primary Energy Supply— From Sunlight," ed, 2010. Used under fair use, 2014.

1.2 Brief History and State of the Art of Solar Cells

Solar cells convert sunlight directly into electrical energy using the concept of photovoltaic effect which was discovered by French physicist Edmond Becquerel in 1839 [4]. When

light consisting of photons strike a semiconductor surface, some of them are absorbed by the electrons in the valence band, which are then excited into the conduction band leaving behind a hole. In a typical photovoltaic device, due to the built-in electric field, these excited electrons and holes are pulled away and collected before they can relax. The first ever large area solar cell was demonstrated by Charles Fritts in 1883 by putting a layer of selenium between gold and another metal [5]. Significant progress in the field of photovoltaic devices began in the early 1960s because of the boost that it received from the space industry owing to the need for power generation on satellites. It was around the same time that researchers started working on silicon electronics, based largely on the concept of silicon p-n junctions. The first silicon solar cell demonstrated at Bell Laboratories had a efficiency of 6% with an estimated cost of $200 per Watt [6]. The obvious application at the time was space where the cost of the cell was unimportant. However, the oil crisis of 1973 experienced by the oil dependent western countries led to renewed focus on photovoltaics for applications other than the space industry. As a result, photovoltaics started becoming competitive in markets where conventional electricity was expensive, for example, remote locations or rural places in developing countries. The potential of solar cells for terrestrial power generation was quickly recognized and this prompted substantial development of the photovoltaic industry.

During the 1980s, solar cell efficiencies began to increase. In 1985, silicon solar cells achieved the milestone of 20% efficiency [7]. Solar cell production increased by 15-30% per annum over the next decade bringing the cost down primarily due to economies of scale. In recent years, further advancements have brought the cost down to almost $1 per

Watt, making terrestrial use of solar cells more feasible. Moreover, novel photovoltaic materials and device architectures have attracted the attention of many researchers.

The holy grail of solar cell research is the achievement of both high power conversion efficiency and low-cost in the same device technology. Most common materials used for solar cell applications are first generation photovoltaics (crystalline and polycrystalline silicon) and second generation photovoltaics (thin film solar cells like GaAs, CdTe, CIGS). Multijunction (MJ) solar-cells which form part of the third-generation photovoltaics offer high efficiencies compared with traditional single junction solar cells. Recently, organic solar cells have received much attention. A comprehensive review of the current state of PV technologies has been compiled by Miles et al [8].

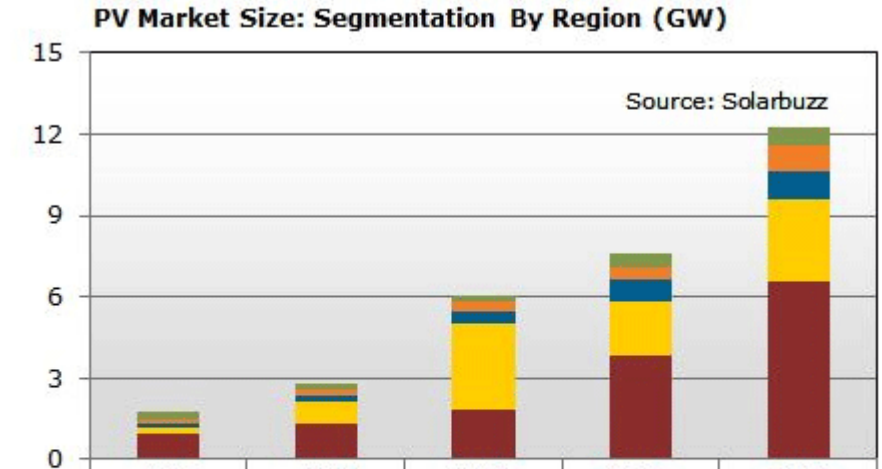

	2006	2007	2008	2009	2010
JPN	0.30	0.23	0.23	0.48	0.62
USA	0.14	0.22	0.36	0.49	0.97
ROW	0.15	0.22	0.50	0.81	1.02
ROE	0.18	0.82	3.13	1.94	3.01
GER	0.97	1.33	1.86	3.87	6.60

Figure 1.4 Annual PV Installations, Solar Energy Market Growth. Available: http://www.solarbuzz.com/facts-and-figures/markets-growth/market-growth. Used under fair use, 2014.

PV Technology has grown at a remarkable rate over last few decades. The world's cumulative PV capacity surpassed the impressive 100-gigawatt (GW) installed electrical power mark, achieving just over 102 GW in the year 2012 [9]. Annual PV installations has increased from a little less than 2 GW in 2006 to almost 12 GW in 2010 as shown in *Figure 1.4* [10]. The photovoltaic solar industry generated $38.5 billion in revenues in the year 2009; and the solar electric energy demand has grown by 30% per annum in the past two decades [10]. Despite the rapid rate of growth, the current global PV market is less than 1% of the world energy usage. One of the primary reasons for this small share in the world energy market can be attributed to high price of solar-generated electricity compared to other energy sources.

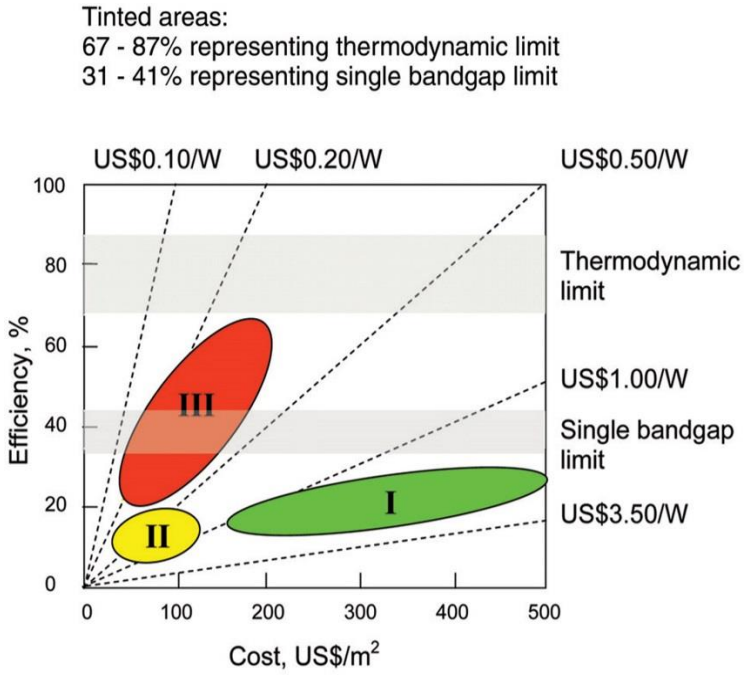

Figure 1.5 Efficiency and cost projections for first, second, and third-generation PV technologies, M. A. Green, Third Generation Photovoltaics: Advanced Solar Electricity Generation," Berlin: Springer-Verlag, 2003. Used under fair use, 2014.

In order for photovoltaics to become economically viable, PV devices must achieve higher conversion efficiencies while maintaining low costs of production and installation. This

leads to the concept of "third-generation" PV having efficiencies greater than single junction solar cells, while retaining the low cost of second generation photovoltaics. The goal of third-generation PV is to achieve cost efficiency better than the $1/W target as shown in *Figure 1.5*, which is equivalent to the price of fossil-based electricity [11].

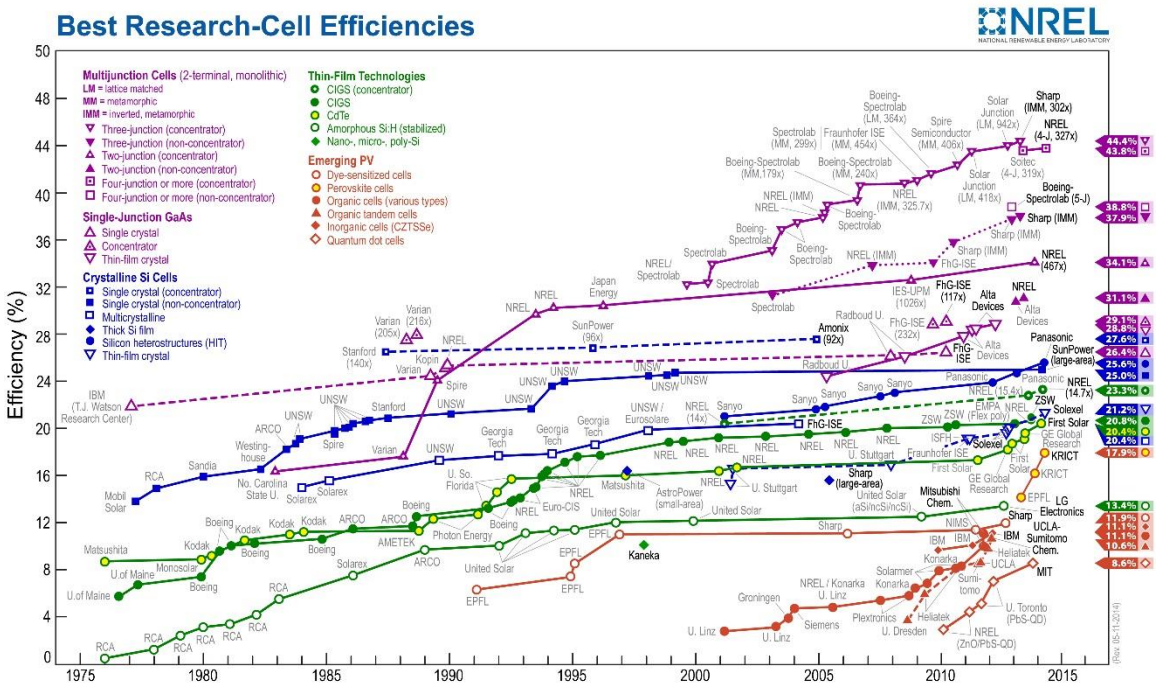

Figure 1.6 Best Research-Cell Efficiencies, Best Research Cell Efficiencies. Available: http://www.nrel.gov/ncpv/. Used under fair use, 2014.

The best research-grade solar cell power conversion efficiencies are summarized in *Figure 1.6 [12]*. The highest confirmed terrestrial efficiencies measured under AM 1.5 conditions at 25 degrees are 25% for single-crystal silicon solar cell; and 28.8% for a thin film GaAs solar cell [13]. Multi-junction solar cells measured under concentrated sunlight are the dominant technology in terms of conversion efficiency. The current efficiency record is held by Sharp Corporation. The efficiency of their concentrator-triple junction solar cell (InGaP top, GaAs middle, and InGaAs bottom) is 44.4% [12]. However, performance of

such multi-junction solar cell are slowly reaching their thermodynamic limits for power conversion efficiencies.

In order to overcome the 50% conversion efficiency barrier, new materials must be explored. The Indium Gallium Nitride (InGaN) semiconductor alloy offers the potential to develop ultra-high efficiency solar cells. The advantages and limitations of this material system are discussed in the following section.

1.3 Indium Gallium Nitride Solar Cell

1.3.1 InGaN Material System

n	**Values of Band Gap (eV)**	**Efficiency (%)**
3	0.7, 1.32, 2	56.0
4	0.60, 1.11, 1.69, 2.48	62.0
5	0.53, 0.95, 1.40, 1.93, 2.68	65.0
6	0.47, 0.84, 1.24, 1.66, 2.18, 2.93	67.3
7	0.47, 0.82, 1.19, 1.56, 2.0, 2.5, 3.21	68.9
8	0.44, 0.78, 1.09, 1.4, 1.74, 2.14, 2.65, 3.35	70.2

Table 1.1 Values of band gap and efficiency for tandems with three to eight junctions calculated at 500X with a black body spectrum at 6000K, W. Shockley and H. J. Queisser, "Detailed Balance Limit of Efficiency of p-n Junction Solar Cells," Journal of Applied Physics, vol. 32, pp. 510-519, 1961. Used under fair use, 2014.

One of the key requirements to achieve conversion efficiencies greater than 50% is the need for a material with band gap greater than 2.4 eV [14]. Optimum values for band gaps of multi-junction solar cells calculated using the detailed balance modeling are presented in *Table 1.1* [15, 16]. The maximum reported conversion efficiency of 44.4% is achieved

by a InGaP-GaAs-InGaAs multi-junction solar cell [12]. According to *Table 1.1*, the highest theoretical efficiency of a triple junction solar cell is 56%. However, it is observed that mature PV technologies are typically able to achieve about 80% efficiencies of their thermodynamic limit [17]. Hence, to achieve conversion efficiencies greater than 50% in practice, multi-junction solar cells having four or more band gaps may be required. Therefore, the need for material systems that have band gaps greater than 2.4 eV arises as evident from the data shown in *Table 1.1*. With the revision of the band gap of InN from 1.9 eV to 0.7 eV [18, 19], the InGaN system now covers an unusually wide energy range (0.7 eV to 3.4 eV) relative to the solar spectrum as shown in *Figure 1.7 [20]*. This suggests the possibility of multi-junction solar cells using InGaN alloys with a continuum of band gaps that can be obtained by changing just the Indium composition.

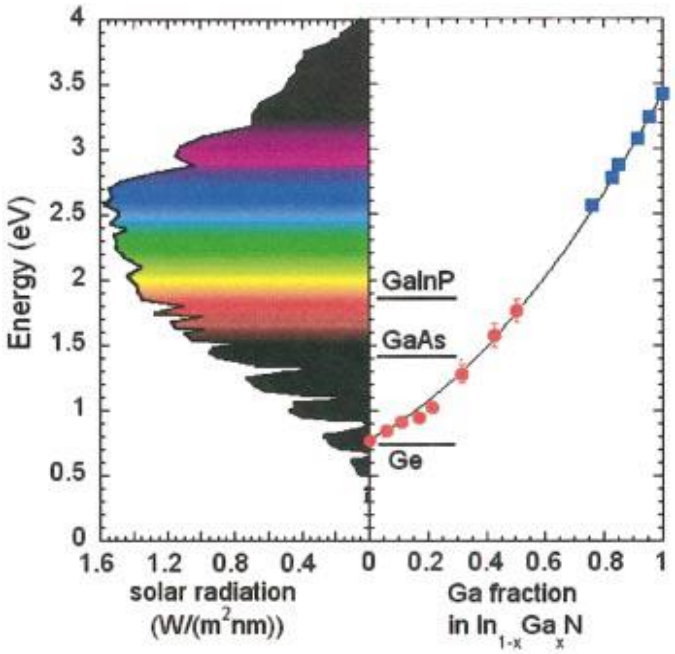

Figure 1.7 Band gap energies of the InGaN alloy system cover the entire air-mass-1.5 solar spectrum, J. Wu, W. Walukiewicz, K. M. Yu, W. Shan, J. W. Ager, E. E. Haller, et al., "Superior radiation resistance of In[sub 1−x]Ga[sub x]N alloys: Full-solar-spectrum photovoltaic material system," Journal of Applied Physics, vol. 94, p. 6477, 2003. Used under fair use, 2014.

InGaN has been widely used for various optoelectronic devices including laser diodes and light-emitting diodes [21-24]. InGaN has high potential for solar cell applications due to superior optical properties [25, 26]. InGaN is a direct band gap semiconductor which means that the creation of electron hole pairs does not require participation of crystal lattice vibrations which wastes energy [27]. InGaN also has a high absorption coefficient, on the order of 10^5 cm^{-1} especially in the near band-gap region [28]. This would result in the absorption of 99% of all incident photons within the first 500nm of InGaN film which would mean that the cost of the material can be minimized by the use of thin films [29].

Two unique features of InGaN are the presence of large piezoelectric and spontaneous polarization effects. InGaN has highly polar molecules which results in the development of electric fields knows as spontaneous polarization. On the other hand, piezoelectric fields are introduced due to lattice mismatch. Bernardini and Fiorentini have shown that InGaN has an apparent insensitivity to high dislocation densities because piezoelectric and polarization effects introduce fields that counter the effect of dislocations [30, 31].

Apart from the above mentioned properties, InGaN also has additional benefits like high electron mobility [32], high peak and saturation velocities and superior radiation tolerance compared to other III-V semiconductors [20]. Also, InGaN solar cells do not contain toxic elements like cadmium, arsenic or phosphorous which are present in other PV technologies being currently used. These potential advantages are driving immense scientific interest in this material system.

1.3.2 Research Progress in InGaN Solar Cells

As explained earlier, the InGaN material system is a promising candidate for developing high-efficiency PV systems. Research involving InGaN photovoltaic devices is still in its initial stages. Since the first proposal in 2003 to use InGaN for solar cell applications, substantial efforts have already been made in this research space [16]. The first device showing PV response was reported in 2007 [29]. With a surging interest in InGaN solar cells, a diverse collection of device structures have been grown and fabricated by various groups. These include p-i-n homo-junction cells [33, 34], p-i-n hetero-junction cells [29, 35-42], InGaN/Si hetero-junction cell [43, 44], InGaN quantum well solar cells [45, 46] and InGaN superlattice cells [47]. However, a variety of challenges associated with this material system (which will be discussed in the next section) have limited the best conversion efficiencies to around 3-4%. A comprehensive review of the current state of the art InGaN based PV devices has been compiled by Bhuiyan et al [48]. The following section will summarize the difficulties and challenges that are limiting the performance of current InGaN based solar cells.

1.3.3 Challenges with InGaN Solar Cells

The InGaN material system is still in the exploratory and developing stages; and therefore, there are a lot of challenges that need to be addressed regarding this material system. The problems can be subdivided in two categories: material based issues and device based issues. The issues associated with material quality include the following: (1) achieving p-type conductivity in InGaN alloys, (2) high dislocation density, (3) phase separation and (4) large lattice mismatch with currently used substrates. The issues related to device design include: (5) making ohmic contacts to p-type InGaN (or GaN) and (6) searching for a suitable transparent current spreading layer. While, some progress has been made towards

addressing these shortcomings, a number of challenges still exist. The present work will focus on issue (6) by introducing a novel Schottky structure consisting of a semi-transparent metal layer (also known as the transparent conductive film) combined with a semiconductor absorber region.

1.4 Research Objectives

A number of groups have recently investigated InGaN-based homo-junction and hetero-junction p-i-n solar cells. However, very few groups have worked on InGaN Schottky solar cells [49, 50]. Compared to p-n junctions, Schottky barrier solar cells are cheaper to grow and fabricate; they are also expected to improve the spectral response because of near surface depletion regions in the shorter wavelength regions. Moreover, the difficulty of growing good quality p-type InGaN has been well documented in literature. Recent efforts to grow p-type InGaN films have resulted in highly resistive films with current crowding effects [51, 52]. A transparent conducting layer is, therefore, necessary for InGaN p-n junction solar cells in order to offset the large resistance of the p-type film. Transparent conducting layers which are usually semitransparent ultra-thin metal films or metallic oxides also known as transparent conducting oxides (TCO) are typically placed in direct contact with the p-side of p-n junction devices and thus must exhibit ohmic behavior with low contact resistance to such materials. These transparent conducting films are combined with an opaque contact grid/finger pattern (covering less than or equal to thirty percent of the surface area) in order to further reduce series resistance. A semi-transparent oxidized layer of Ni-Au has been widely reported in literature as a current spreading layer for InGaN p-n junction solar cells.

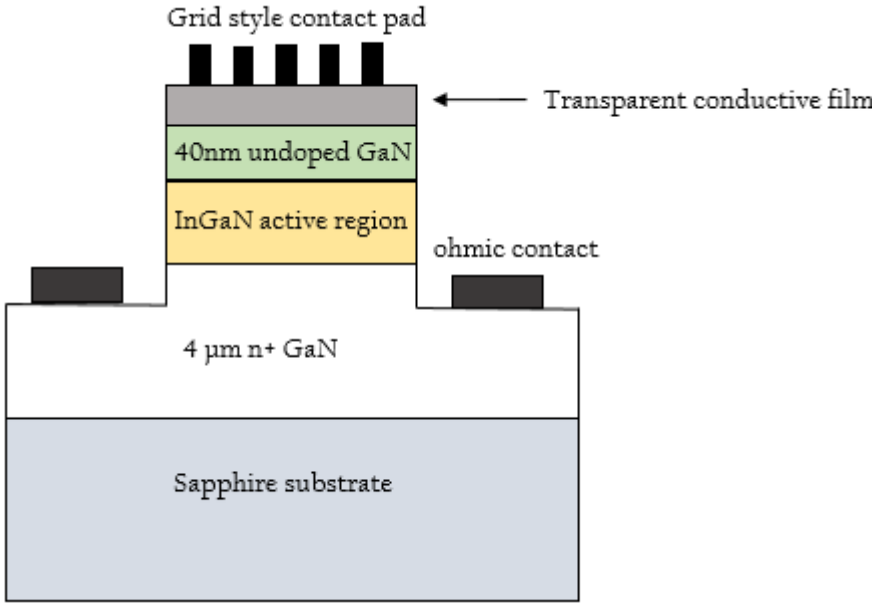

Figure 1.8 Schottky InGaN-GaN Solar Cell Structure

In the present work, the issue of poor quality p-type InGaN was circumvented by using a Schottky barrier instead of a p-n junction to extract photo-generated carriers. The Schottky diode structure is shown in *Figure 1.8.* For the devices considered herein, the transparent conductive film is one side of the Schottky diode structure as can be seen in *Figure 1.8*. There is a clear trade-off between the amount of incident light transmitted through this transparent conductive film into the cell and the fraction of photo-generated carriers that are extracted by it. In this study, platinum (Pt) is used to form a Schottky contact with n-type InGaN/GaN absorber layers which also serves as the transparent conductive film. Pt is used as the transparent conductive film because it is a well understood metal and it forms a Schottky barrier with n-type GaN with good rectifying characteristics. Results derived from this work with Pt will be useful in improving the understanding of InGaN Schottky solar cells and how this transparent conductive film affects device performance. This work will also serve as a reference for InGaN Schottky solar cells fabricated with other types of

transparent conductive films. In this study, electrical and optical properties of platinum films of varying thicknesses are investigated. We also report the photovoltaic properties of InGaN/GaN Schottky solar cell with platinum as the transparent conductive film. The relationship is studied as a function of the thickness of the metal. Different contact schemes are employed (layer and grid contacts). An effort is made to explain the impact of these contact schemes on solar cell performance.

1.5 Organization of Thesis

In *Chapter 2*, the physics of solar cells with a particular focus on the theory of Schottky solar cells is discussed at length. The theory of metal semiconductor contacts and concepts of optical transmission and absorption for semiconductors as well as for thin metal films are discussed. *Chapter 3* describes characterization methods and parameter extraction techniques used to evaluate the electrical and optical properties of thin metal films. It also presents a summary of the results. In *Chapter 4*, solar cell characterization techniques and our results are presented. *Chapter 5* concludes the thesis, the results are summarized and the scope of this research is presented.

Chapter 2. Schottky Barrier Solar Cells: Principles of Operation

2.1 Theory of P-N Junction Solar Cells

A solar cell is a device which converts sunlight into electricity. The cell is a two terminal device that behaves like a diode in the dark and generates a photocurrent in the presence of light. The basic principle behind its operation is the photovoltaic effect. When light made of packets of energy, called photons strike the surface of the cell, photons with energies greater than the band-gap, E_g, of the absorbing material get absorbed while the photons with energies less than E_g pass through the material. Each photon absorbed by the solar cell, excites an electron from the valence band to conduction band, thus creating an electron-hole pair. Electrons generated in the p-type material and holes in the n-type material are "minority carriers" and thus will only exist for a duration of time equal to the minority carrier lifetime before they recombine. If recombination occurs, then no electrical power will be generated. Instead the goal is to have these minority carriers diffuse through the quasi-neutral regions until they reach the p-n junction as shown in *Figure 2.1*. The minority carriers are then swept across the p-n junction by the action of the electric field existing across the depletion region. The electrons move towards n-side, while the holes move towards the p-side. Once the photo-generated electrons (holes) reach the n-side (p-side) of the junction they contribute to the majority carrier currents in these regions. In essence, photovoltaic action results from three steps which are charge generation (photons generating electron-hole pairs), charge separation, and charge transport. Due to the presence of these excess carriers, a voltage is set up across the junction which splits the equilibrium Fermi-level into two quasi-Fermi levels, one for electrons ($E_{f,n}$) and the other

for holes ($E_{f,p}$) shown in *Figure 2.1*. When the contacts to the cell are isolated, the potential difference across the diode has its maximum value which is equal to the open-circuit voltage (V_{oc}). If the solar cell is short-circuited, the current density that flows is known as the short-circuit current density (J_{sc}).

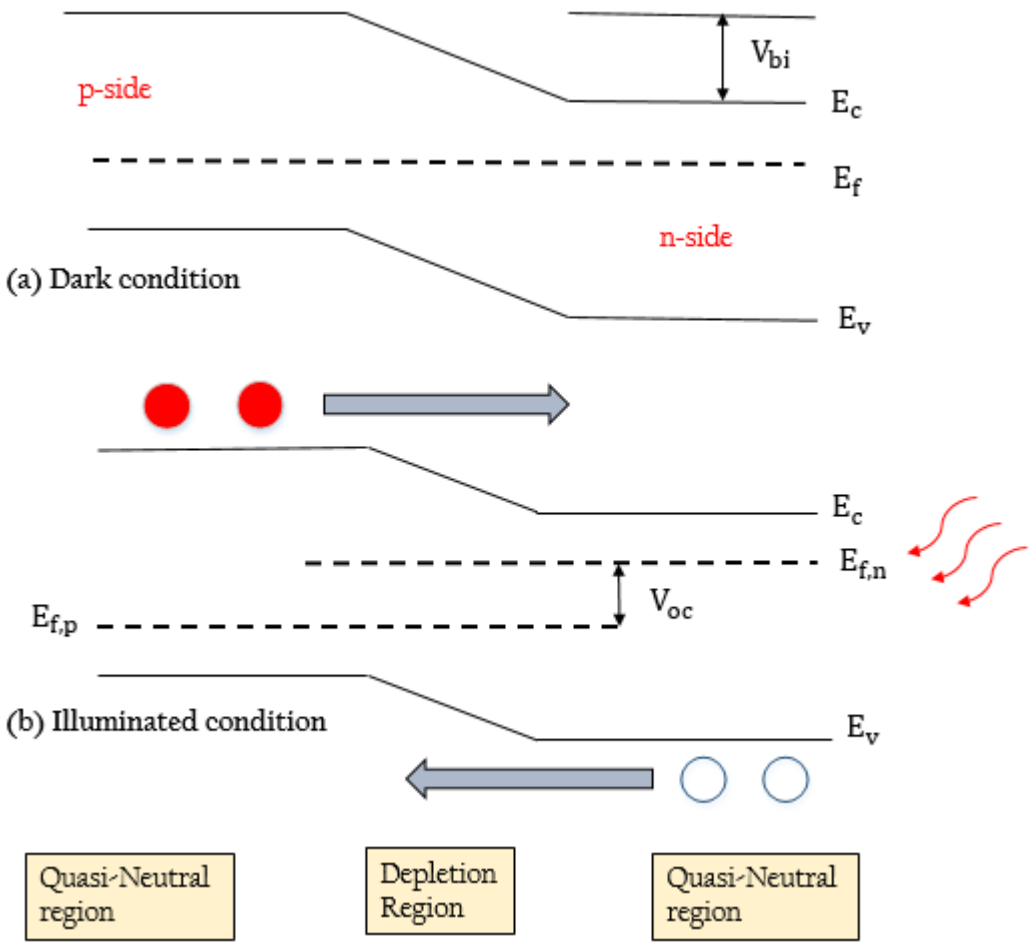

Figure 2.1 Band diagram of an unbiased p-n junction solar cell (a) in the dark (b) under illumination

The net current density delivered, J, by a solar cell to a resistive load is:

$$J(V) = J_{sc} - J_{dark}(V) \tag{2.1}$$

where J_{dark} is the dark current density. For a non-ideal diode, J_{dark} is given by:

$$J_{dark}(V) = J_0(e^{qV/nk_BT} - 1) \tag{2.2}$$

Thus, J becomes:

$$J(\mathrm{V}) = \mathrm{J_{sc}} - \mathrm{J_0}(\mathrm{e}^{\mathrm{qV/nk_BT}} - 1) \tag{2.3}$$

where V is the voltage across the diode, J_0 is the saturation current density, n is the ideality factor of the diode, $k_B$is the Boltzmann constant and T is the temperature. The "open-circuit" condition is defined by $J(V_{oc}) = 0$ and therefore we can rearrange Equation 2.3 to find $\mathrm{V_{oc}}$, which is given by:

$$\mathrm{V_{oc}} = \frac{\mathrm{nkT}}{\mathrm{q}} \ln\left(\frac{\mathrm{J_{sc}}}{\mathrm{J_0}} + 1\right) \tag{2.4}$$

Equation 2.4 shows the relationship between open-circuit voltage and the short circuit current. The open circuit voltage can also be thought of as the difference between the quasi-Fermi levels across the p-n junction, and thus, it is limited by the band gap of the semiconductor as show in *Figure 2.1*.

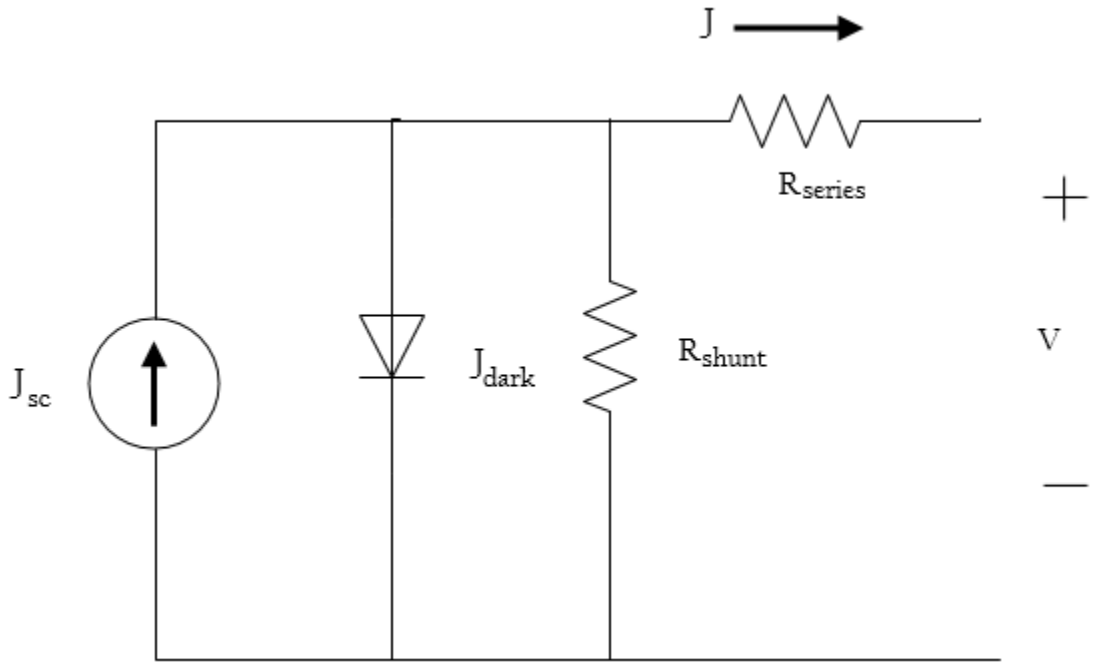

Figure 2.2 Equivalent circuit of a non-ideal solar cell

Such an ideal solar cell can be represented by a current source in parallel with a diode. A more realistic equivalent circuit model, including series and shunt resistances is shown in *Figure 2.2* [7]. The net current density taking into account the series and shunt resistance is given by the following equation:

$$J = J_{sc} - J_0\left(e^{\left(\frac{q(V-J.R_{series})}{nkT}\right)} - 1\right) + \frac{V - J.R_{series}}{R_{shunt}} \quad (2.5)$$

where R_{series} and R_{shunt} represent specific resistances with Ωcm^2 as their units. In non-ideal solar cells, power is dissipated through the series and shunt resistances included in *equation 2.5*. The total series resistance has contributions from the bulk semiconductor material, the contact resistance associated with the semiconductor/metal interface and the resistance of the front and rear metal electrodes. Shunt resistance arises primarily from electrically active defects introduced either during materials synthesis or device fabrication. Both series and shunt resistances have a detrimental impact on the fill factor (explained in the next paragraph) and hence, the overall efficiency of a solar cell. The power density delivered by a solar cell to a resistive load is given by:

$$P = J.V \quad (2.6)$$

The open-circuit voltage (I = 0) and short-circuit (V = 0) current are labeled on the prototype solar cell J-V curve shown in *Figure 2.3*. However, no power is generated at these two points. The power density in a solar cell reaches its maximum value at some voltage $V_m$with a corresponding current density of J_m. The maximum power is calculated by setting the derivative of power density equal with respect to voltage to zero.

$$\frac{dP}{dV} = 0 \quad (2.7)$$

The fill factor is an important parameter that determines the maximum power that can be drawn from a solar cell. The fill factor is defined as the ratio:

$$FF = \frac{J_m . V_m}{J_{sc} . V_{oc}} \tag{2.8}$$

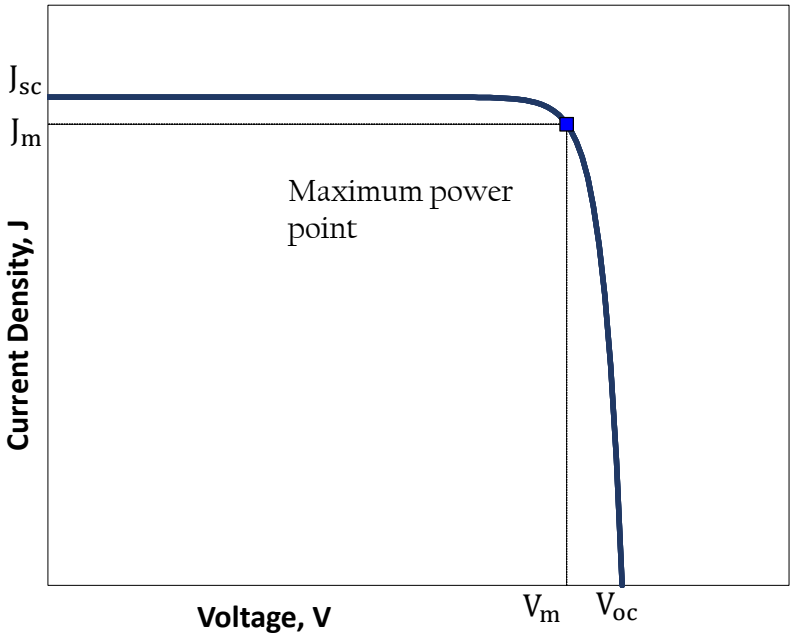

Figure 2.3 Current voltage characteristic of an ideal cell

Graphically, the fill factor describes the 'squareness' of the J-V plot in the sense that with $V_m = V_{oc}$ and $J_m = J_{sc}$, the J-V curve would outline a rectangle and FF = 1. It also represents the largest rectangle that can be inscribed inside the J-V curve shown in *Figure 2.3*. The efficiency η of a solar cell is defined as the ratio of the maximum power density delivered to the load and the incident light power density, P_{inc}:

$$\eta = \frac{J_m . V_m}{P_{inc}} = \frac{J_{sc} . V_{oc} . FF}{P_{inc}} \tag{2.9}$$

These quantities J_{sc}, V_{oc}, FF and η are the essential "device metrics" of a solar cell. In order to make useful comparisons of solar cell performance, these parameters should be

measured under "standard" illumination conditions. The standard spectrum at the Earth's surface is AM1.5G (the G stands for global and includes both direct and diffuse radiation) or AM1.5D (which includes direct radiation only) [7]. The standard spectrum outside the earth's atmosphere is AM0 (air mass zero).

Quantum efficiency is an important diagnostic quantity in that its spectral dependence can be used to identify shortcomings in material quality and/or layer structure design. The external quantum efficiency (EQE) of a solar cell is the ratio of the number of carriers flowing through the electrical circuit to the number of photons incident on the solar cell. The internal quantum efficiency (IQE) of a solar cell is obtained from the EQE by including only absorbed photons (i.e. by subtracting out photons lost to reflection or transmission from the incident light intensity). A sample quantum efficiency curve is shown in *Figure 2.4*. As seen in *Figure 2.4*, the quantum efficiency is reduced due to recombination effects. It is also affected by short diffusion lengths and reflections occurring at the top surface.

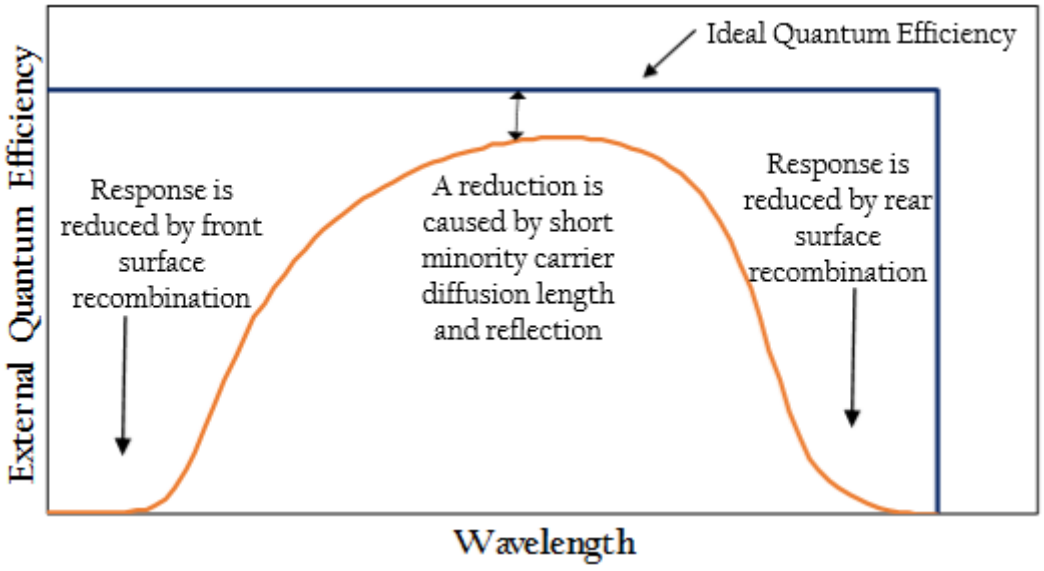

Figure 2.4 Quantum Efficiency of a sample solar cell

The impact of carrier recombination on solar cell performance is represented by two quantities which are minority carrier lifetime and diffusion length. Minority carrier lifetime (τ) is the average time which a photo-generated carrier spends in an excited state before it recombines.

$$\frac{1}{\tau} = \frac{1}{\tau_{\text{radiative}}} + \frac{1}{\tau_{\text{auger}}} + \frac{1}{\tau_{\text{SRH}}} \tag{2.10}$$

where $\tau_{radiative}, \tau_{auger}$ and τ_{SRH} represent minority carrier lifetimes as a result of radiative, Auger and Shockley-Read-Hall recombination mechanisms [5]. In the radiative process, an electron from the conduction band recombines with a hole in the valence band and releases a photon. Recombination through point defects occurs via the Shockley-Read-Hall mechanism which is a two-step process. An electron is trapped by an energy state within the band-gap which is due to defects present in the crystal lattice. If a hole moves up to the same energy state before the electron is re-emitted, then the electron and hole recombine. In Auger recombination, three particles are involved. First, the electron recombines with a hole to give out energy which is then given to an electron in the conduction band (hole in the valence band) pushing it high into the conduction (valence) band. The excited electron (hole) gradually loses that energy thermally to come back to the edge of the conduction (valence) band.

Diffusion length (L) is the average distance a carrier diffuses in a concentration gradient from the point of generation until it recombines.

$$\mathrm{L} = \sqrt{\mathrm{D}\tau} \tag{2.11}$$

where D is the diffusion coefficient and can be found using

$$D = \mu \frac{kT}{q} \tag{2.12}$$

The value of τ depends on the number of defects in the bulk material via the SRH term in *Equation 2.10*. Also, since the surface of a solar cell presents a disruption of the lattice, the surface is a site of particularly high recombination. Surface recombination velocity is the parameter which is used to quantify recombination at the surface. The recombination of charge carriers has a major impact on the open circuit voltage of the solar cell. High recombination increases the forward-bias recombination current of the diode, which in turn decreases the open circuit voltage of the solar cell. It can be seen how parameters like diffusion length and surface recombination affect the quantum efficiency of a solar cell in *Figure 2.4*.

2.2 Theory of Schottky Barrier Solar Cells

The energy band diagram for a Schottky barrier (metal/n-semiconductor) solar cell is shown in *Figure 2.5*. The metal is deposited as a semi-transparent film through which most of the light can pass. Light transmitted through the metal into the semiconductor is absorbed to generate photocurrent. A very small part of the photocurrent is also contributed by light absorption in the thin metal layer (although this photocurrent is negligible and is not considered in the analysis). The current density versus voltage characteristic of a Schottky barrier solar cell under illumination is similar to *Equation 2.3* for the p-n junction, which is restated here:

$$J = J_{sc} - J_0(e^{qV/nk_BT} - 1) \tag{2.13}$$

where J_0, the saturation current density, is now given by:

$$J_0 = A^{**}.T^2.\exp(-q.\varphi_b/k_b.T) \quad (2.14)$$

where A^{**} is known as the Richardson constant and φ_b is the Schottky barrier height.

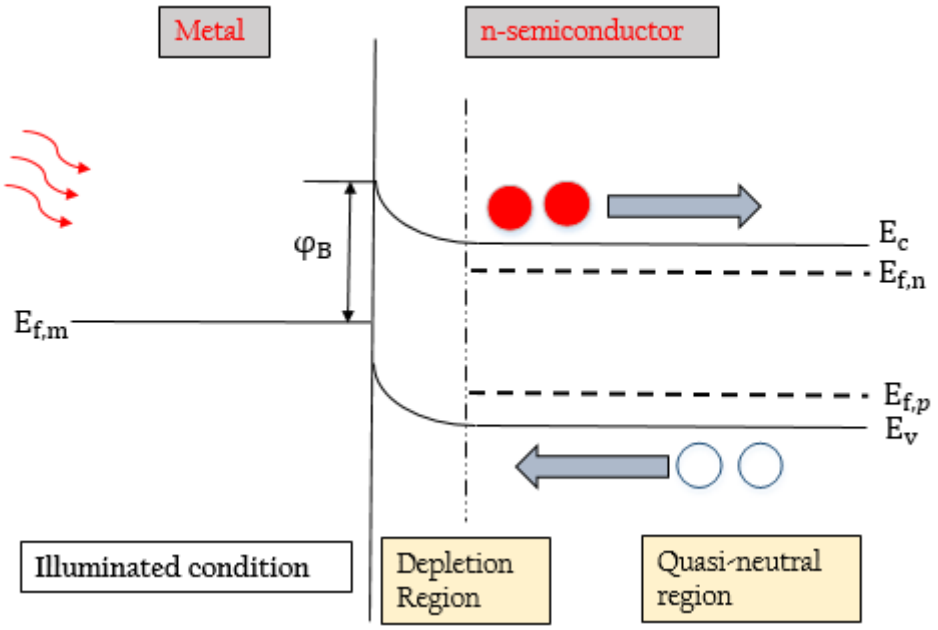

Figure 2.5 Energy band diagram of Schottky Barrier Solar Cell under illumination

The metal-semiconductor junction (Schottky diode) is a simple way to prepare a photovoltaic device. The other main advantage of a Schottky barrier solar cell is the presence of the depletion region right next to the metal surface which reduces the surface recombination probability and thus, improves the spectral response for high energy photons. However, Schottky barrier solar cells have a few limitations. A Schottky barrier solar cell cannot produce high open circuit voltages because the maximum value is limited by the potential energy difference between the metal work function and semiconductor electron affinity. Whereas, for a p-n junction solar cell, the open circuit voltage can be roughly x% of the semiconductor band-gap. Secondly, in the case of highly doped semiconductors, thin barrier layers may result in tunneling of carriers which will reduce

the photocurrent. Moreover, the material interface between the semiconductor and metal contains interface states which may trap charge and reduce the open circuit voltage.

2.3 Solar Cells with Transparent Conducting Films

One of the most important design considerations for both Schottky and p-n junction solar cells is to minimize resistive losses. As explained before, series resistance arises due to material properties and electrode design. In order to decrease the material resistance, doping can be increased which also enhances the electric field to help in carrier collection. However, for a Schottky structure, increased doping may result in tunneling which reduces the net photocurrent. Electrode resistance is generally reduced by increasing the dimensions and thickness of metal fingers or grid patterns used as the top electrodes. This, however, is done at the cost of reducing the transmission of light entering the cell. Careful optimization of the line-width and grid-spacing is required in order to improve efficiencies.

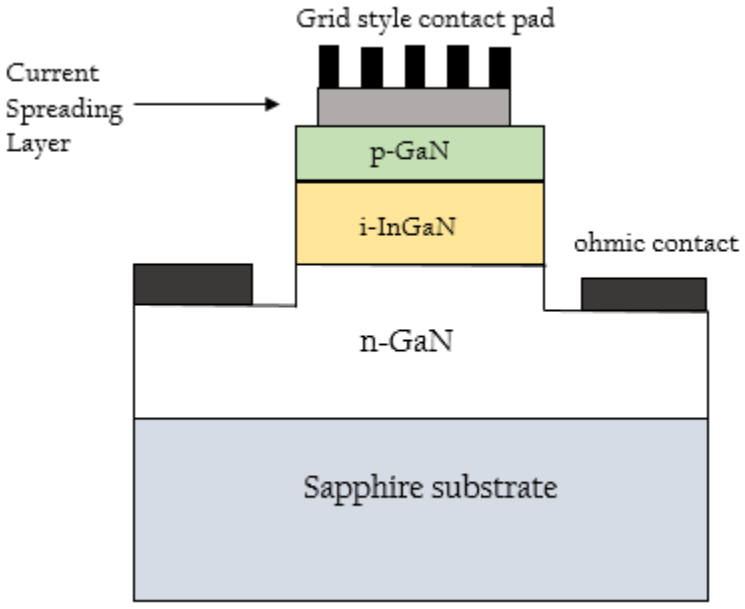

Figure 2.6 InGaN-GaN p-i-n junction solar cell structure

Transparent conducting layers which are usually thin (semitransparent) metal films or metallic oxides (also known as transparent conducting oxides or TCOs) are used as current spreading layers between the top metal electrode and the p-side of the p-n junction, as shown in *Figure 2.6*. These layers are especially important in InGaN p-n junction solar cells because of the large resistance associated with p-type GaN films. The current spreading layer has a strong influence on the performance of InGaN p-n junction solar cells. In addressing this issue, a semi-transparent oxidized layer of Ni-Au has been widely reported in literature as a current spreading layer. However, there are very few reports on the issue of optimizing this layer or looking for other options. A couple of papers have reported the effect on photovoltaic response by using ITO instead of Ni-Au current spreading layers [53-55].Neufeld also demonstrated that the performance of InGaN p-n junction solar cells can be improved by optimizing the metal electrode grid spacing [35].

In the present work, a transparent conductive film has been used to form a Schottky barrier with the InGaN/GaN absorber region, thus, forming an active part of the solar cell shown previously in *Figure 1.8*. Ultra-thin metal films of Pt have been used as the transparent conductive material. This work will investigate the feasibility of InGaN based Schottky solar cells with Pt serving as both the Schottky barrier "metal" and the current spreading layer.

2.4 Metal-Semiconductor Contacts

The energy band diagram of a metal-semiconductor contact at equilibrium is shown in *Figure 2.7*. Metal semiconductor contacts form an important part of all semiconductor

devices. A metal-semiconductor junction results in either an ohmic contact or Schottky barrier. In an ohmic contact, there is a linear relationship between current and voltage (for both voltage polarities) and the goal is to minimize the voltage drop for a desired current flow. The contact resistance should be as small as possible in comparison to the bulk resistance of the semiconductor. The current-voltage curve of an "ohmic" contact should ideally be linear. However, in practice, the current-voltage curve of an ohmic contact does not have to be exactly linear in order for it to be useful. In a Schottky barrier or rectifying contact, current is blocked for one polarity of voltage. Thus, the current voltage curve of a Schottky contact should be rectifying in nature like a diode.

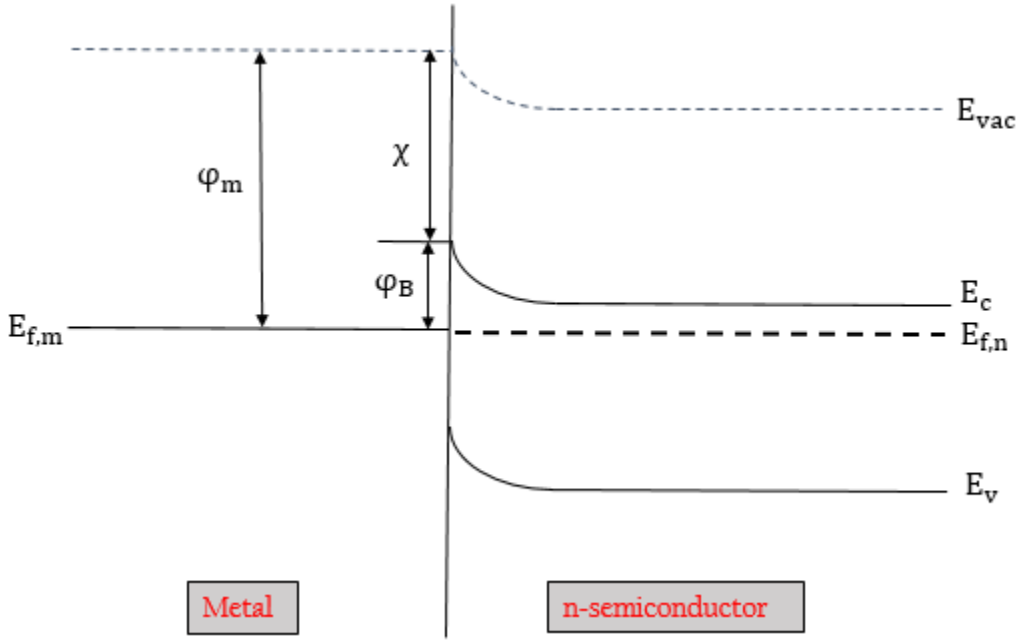

Figure 2.7 Band Diagram of metal-semiconductor contact

The Schottky barrier height of a metal/ n-type semiconductor interface is given by:

$$q.\varphi_{B,n} = q.(\varphi_M - \chi) \qquad (2.15)$$

where, $\varphi_{B,n}$ is the barrier height, $\varphi_M$is a the work function of metal and χ is the electron affinity of the semiconductor. For an n-type semiconductor, in order to make an ohmic contact, the work function of the metal must be smaller than the electron affinity of the semiconductor. For a p-type semiconductor, the formation of an ohmic contact requires the work function of the metal to be larger than the sum of the electron affinity and the band gap energy. Since the maximum value of work function for known metals is just above 5 eV and a typical value of electron affinity is about 4 eV, it is extremely tough to find metals that form ohmic contacts to p-type semiconductors with wide band gaps such as GaN [56, 57]. Notwithstanding this situation, Ho demonstrated that Ni-Au layers when annealed in oxygen ambient make ohmic contacts to p-type GaN with specific contact resistances as low as $10^{-6}\Omega.cm^{-2}$ [58, 59]. It is important to recognize that TCOs that form good ohmic contacts to *p-type* GaN and *p-type* InGaN should yield Schottky barriers to n-type GaN with large values of $\varphi_{B,n}$.

2.5 Absorption and Transmission in Thin Films

The process of fundamental or band-to-band absorption refers to photons exciting an electron transitions from the valence band to the conduction band in a semiconductor (or lower filled band to higher empty band in a metal or metal oxide film). A bulk semiconductor's optical absorption coefficient α can be calculated from its optical transmission data. When light of intensity I_0 is incident on a film of thickness x, a transmitted intensity I emerges out of the other side. Beer Lambert's law states that there is a logarithmic relation between the absorption coefficient and the transmitted optical intensity according to the following equation:

$$T = \frac{I}{I_0} = e^{-\alpha x} \tag{2.16}$$

where, α is the absorption coefficient at a fixed wavelength. This equation assumes there is no scattering of light within the semiconductor film. This equation also does not take into account power reflection/transmission at the top and bottom film surfaces. Accounting for multiple reflections that occur at the film surfaces, the transmission coefficient $T = I/I_0$ is given by [60]:

$$T = [(1 - R)^2 . exp(-\alpha . x)]/[1 - R^2 . \exp(-2 . \alpha . x)] \tag{2.17}$$

where, R is power reflection coefficient at the air-film interface, given by:

$$R = [(n - 1)^2 + k^2]/[(n + 1)^2 + k^2] \tag{2.18}$$

Note that the equation treats the air/film and air/substrate interface the same. *Equations 2.17* and *2.18* are used to calculate the absorption coefficient of thin films using the optical transmission and reflection data.

TCO materials are not typically used as current spreading layers in III-V multi-junction solar cells and crystalline silicon solar cells [61, 62]. The reason for not using a TCO in these solar cells is because they require high transmittance near the infrared region which none of the current TCOs can provide. Transmission in the infrared region is limited by free carrier absorption. Free carrier absorption occurs when a material absorbs a photon and the carrier is excited from a filled state to an unoccupied state within the same band. In a simple Drude theory formulism, the plasma wavelength, λ_p, or the onset of total reflection can be expressed as [63, 64]:

$$\lambda_p = 2\pi c \sqrt{\frac{\varepsilon_\infty m^*}{4\pi n e^2}} \tag{2.19}$$

where ε_∞ is the high frequency permittivity, n is the free electron concentration and m^* of effective mass of the electron which depends on the energy band structure. For wavelengths shorter than λ_p, transmission is limited by free carrier absorption. The dependence of λ_p on the effective mass, and the connection between effective mass and carrier mobility, implies that increasing transmission in the IR region requires TCOs with high mobility. *Equation 2.19 also* shows that materials with low carrier concentrations are required to push λ_p into the UV range where the solar radiation spectrum is relatively weak. However, lowering the electron concentration reduces the conductivity of a material whereas, high conductivity is a desired characteristic of a TCO. The same is true for semi-transparent metals used as transparent conductive layers. Hence, an ideal TCO (or semi-transparent film) requires optimization of optical transparency and electrical conductivity.

The next two sections of this thesis will focus on characterization methods used for this work. There are two parts to characterization methods used in this study. The first part which is summarized in *Chapter 3* focusses on the characterization of thin metal films of Pt which will be used as the transparent conducting layer in our Schottky barrier solar cell. The second part involves solar cell characterization with Pt films serving as the TCO electrode which will discussed in *Chapter 4*.

Chapter 3. Characterization of Transparent Conducting Films

This chapter will present the characterization methods and parameter extraction techniques used to characterize the transparent conducting films which are integral to the Schottky solar cells of interest here. The measurement results will also be presented.

3.1 Transfer Length Measurements (TLM)

Transfer Length Measurements or Transmission Line Measurements is a technique used to determine the contact resistance between a metal and a semiconductor originally proposed by Shockley [65]. However, we will use this technique to calculate the sheet resistance of our thin metal films. This method requires making a series of metal-semiconductor (or thin metal film) contacts separated by increasing distances.

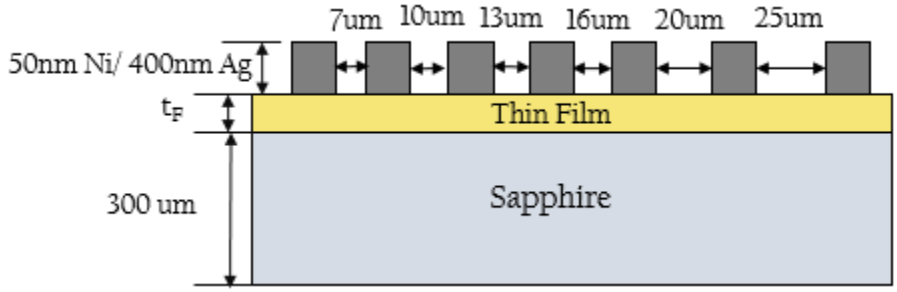

Figure 3.1 Cross-sectional schematic of a representational TLM test pattern

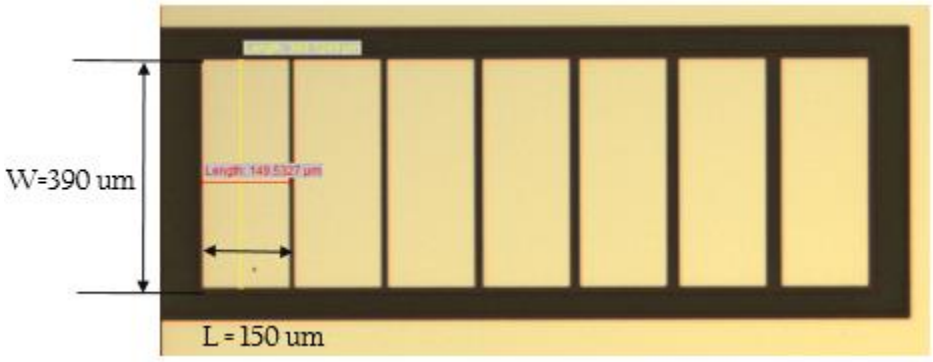

Figure 3.2 Planar view of fabricated TLM patterns

Figure 3.1 is a cross-sectional schematic of a TLM test pattern. The thin film (with thickness equal to t_F) under test is deposited on double side polished sapphire. 50nm of Nickel (Ni) followed by 400nm of Silver (Ag) is used as the ohmic contact layer. *Figure 3.2* is an optical image of a fabricated TLM test pattern. The metal contacts are separated from each other in the following order of distances: 7 μm, 10 μm, 13 μm, 16 μm, 20 μm and 25 μm.

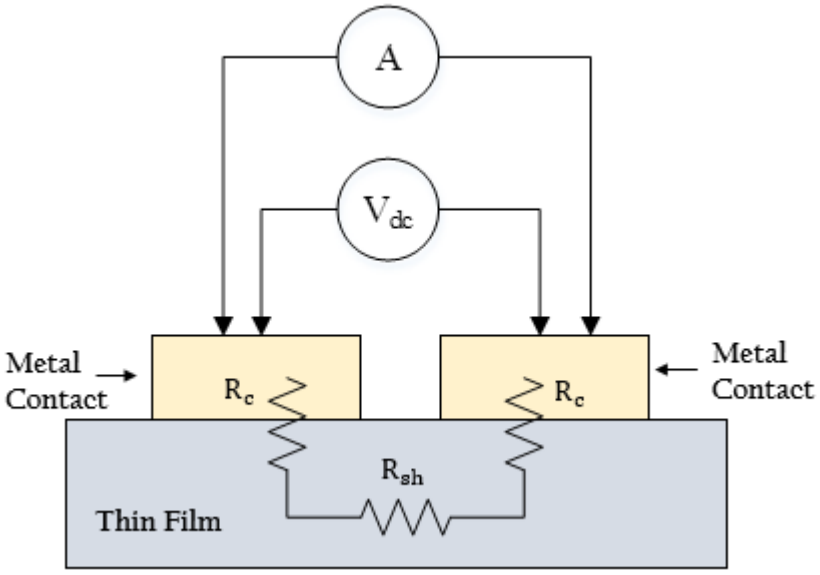

Figure 3.3 Four-point measurement system for TLM measurements

A four-point measurement configuration is used as shown in *Figure 3.3*. The probes are applied to one pair of contacts at a time and then cycled through all the contact pairs in the structure. I-V measurements were made using a Keithley 2400 source meter which is used to ramp the current while simultaneously measuring the voltage drop across the contacts. The resistance measured is a summation of the interfacial metal/film resistance (R_c) of both contacts plus the sheet resistance (R_{sh}) of the thin film. Once resistance measurements are made for all adjacent pairs of contacts, a plot of resistance versus contact separation can be made which should yield in a straight line. The equation is:

$$R_T = \frac{R_{sh}}{W}.l + 2.R_c \tag{3.1}$$

where, R_{sh} is the sheet resistance, W is width of the metal contact, l is the distance between the contacts and R_c is the contact resistance.

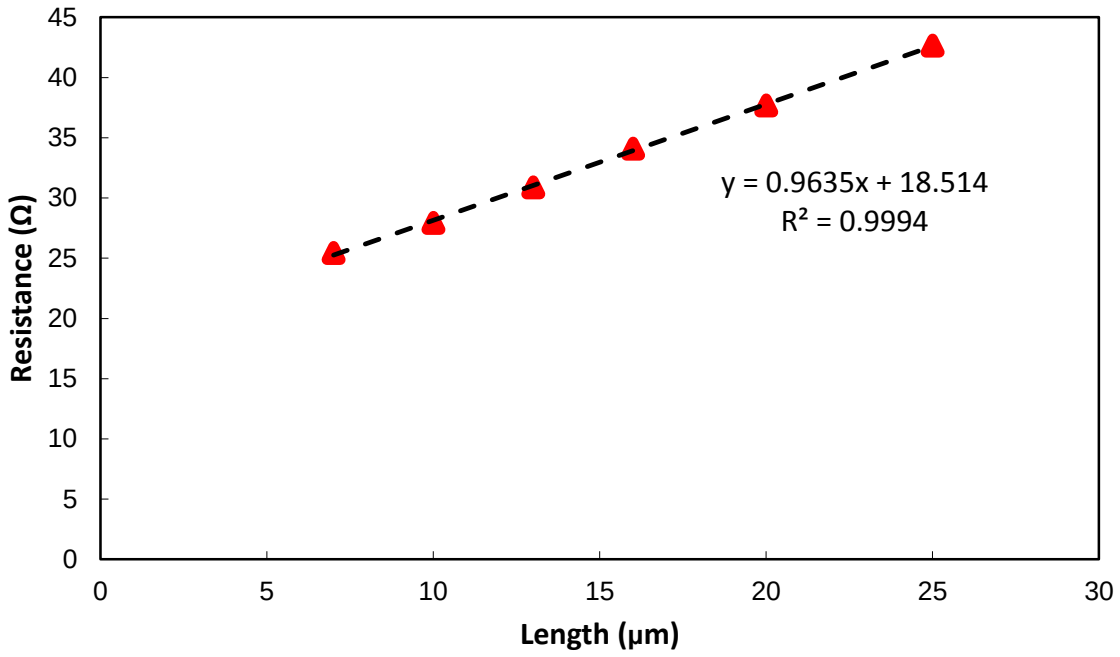

Figure 3.4 Resistance versus Contact Separation

Figure 3.4 is a plot of resistance versus contact separation for representation purposes. The red triangles denote measurement data points and the dotted black line represents a linear fit to the data points. The slope and the y intercept of the line are used to extract the sheet resistance and the contact resistance. The x intercept is equal to twice the transfer length which can be extrapolated from the equation of the line. The transfer length is the average distance that an electron (or a hole) travels in the film beneath the contact before it flows up into the contact. So the effective area of the contact is:

$$A = L_T.W \tag{3.2}$$

The contact resistance can be defined as:

$$R_C = \frac{\rho_c}{L_T . W} = \frac{R_{sh} . L_T}{W} \quad (3.3)$$

While this method is widely used to calculate sheet resistances of thin films and contact resistances of metal contacts; it also makes a few assumptions that we should be aware of. The first assumption is that the contact resistance of all metal contacts are identical. Secondly, the assumption of electrically long contact ($L >> L_T$) enables the relationship $\rho_c = R_{sh} . {L_T}^2$, used in our analysis. Lastly, we assume that the metal contact does not alter the sheet resistance of the thin film which might not always be true. Reeves described a method to calculate the modified sheet resistance and also showed how to deduce specific contact resistance by carrying out an end resistance measurement [65]. However, we will not calculate the modified sheet resistance. The TLM method, described above, will be used herein to determine the sheet resistance of the transparent conductive films (thin Pt films in this case) employed in the Schottky solar cells. Additional details regarding measurement setup and calibration procedure can be found in *Appendix A.*

3.2 Transmission and Reflection Measurements

The two most common techniques for determining film thickness are optical and stylus based measurements. Optical techniques are preferred because they are more accurate and non-destructive. The most common optical measurement systems are spectral reflectance and ellipsometry. Spectral reflectance measures the reflected light from a thin film when light is normally incident on it over a range of wavelengths. Ellipsometry is similar, except that it uses non-normal incident light at two different polarizations. The optical properties of thin films used in this work were studied by using a F10-RTA-UVX Filmetrics Measurement System. The F10-RTA-UVX reflectometer captures reflectance and

transmittance spectra simultaneously across a wide range of wavelengths (200nm-1700nm). The software converts these spectra into thickness and refractive index data. The specifications of the F10-RTA-UVX are shown below in *Table 3.1.*

Specifications	**F10-RTA-UVX**
Wavelength Range	*200-1700 nm*
Thickness Range	*3 nm-150 µm*
Minimum Thickness to measure n and k	*15 nm*
Thickness Accuracy	*1 nm*
Thickness Precision	*0.1 nm*
Thickness Stability	*0.07 nm*
Light Source	*D2+Halogen*

Table 3.1 F10-RTA-UVX Specifications

The Filmetrics measurement system will be used to study the optical characteristics of the thin Pt films which will be used as transparent conductive films in Schottky solar cells. Specifically, we will measure the transmission spectra of these Pt films.

3.3 Data Analysis and Discussion

3.3.1 TLM Results

Platinum films of varying target thicknesses (7 nm, 10 nm and 13 nm) were deposited on double side polished sapphire using electron-beam evaporation with a base pressure lower than 2×10^{-6} Torr. The thickness of the Pt films were measured using a Zygo surface profiler to confirm the thickness deposited, which showed a maximum absolute error of 1 nm. TLM patterns were formed as shown in *Figure 3.1*. The metal film under test was patterned with Ni (50nm) / Ag (400nm) as the metal contact with interspacings of 7 μm, 10 μm, 13 μm, 16 μm, 20 μm and 25 μm. The TLM patterns were defined by a photolithographic lift-off process. I-V measurements between pairs of contacts with

varying distances on the TLM patterns revealed linear behavior for all the three platinum films, which was expected.

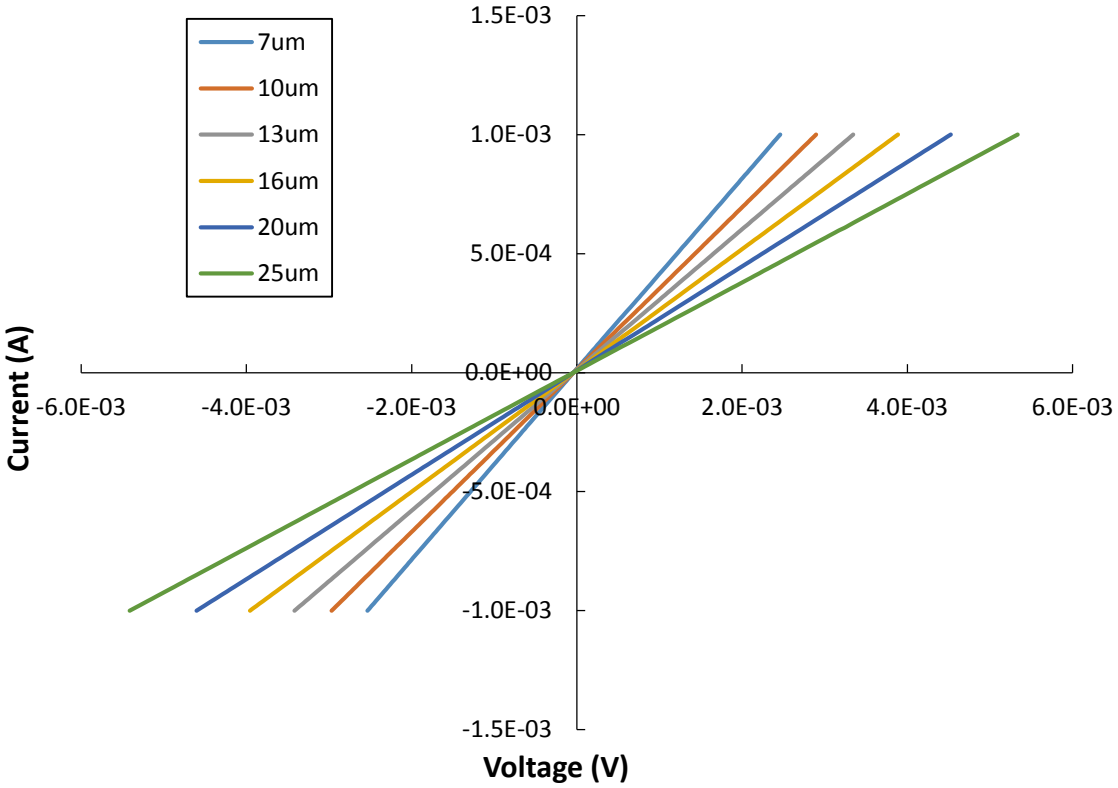

Figure 3.5 I-V Measurements between metal contacts as a function of the distance between them for 10nm Pt sample

Figure 3.5 shows the I-V measurements made across pairs of contacts with varying distances for the sample with a 10 nm thick Pt film. These I-V measurements across pairs of contacts with varied spacing were used to calculate the associated resistances. As can be seen in *Figure 3.5*, the slope of the I-V curves keeps decreasing with increasing distances, which indicates an increase in the resistance as a function of distance, which is expected. These resistance values are then plotted as a function of distance in order to extract the sheet resistance of the Pt film. *Figure 3.6* shows the total resistance versus distance curve for the 10 nm Pt sample for eight different TLM patterns. As can be seen in the figure, all eight TLM patterns show linear behavior with a positive slope.

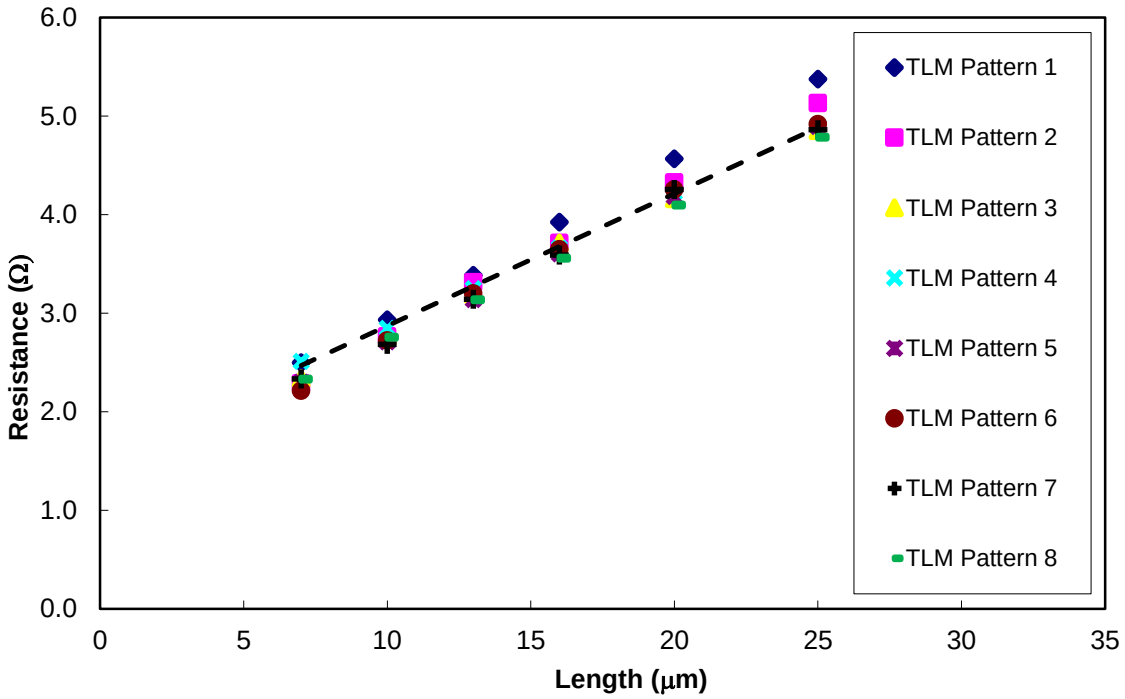

Figure 3.6 Total Resistance versus distance between the contacts for 10 nm Pt sample

The slope and the y-intercept of the straight line fit corresponding to each TLM pattern is used to calculate the sheet resistance of the Pt film. *Table 3.2* shows all the parameters extracted using the techniques described in *Section 3.1*.

TLM Pattern #	Slope (Ω/μm)	y-intercept (μm)	R^2	R_C (Ω)	L_T (μm)	R_{SH} (Ω/sq)
1	0.161	1.333	0.999	0.666	4.133	62.913
2	0.156	1.208	0.998	0.604	3.852	61.196
3	0.140	1.375	0.997	0.687	4.902	54.690
4	0.134	1.527	0.999	0.763	5.686	52.396
5	0.145	1.267	0.999	0.633	4.363	56.650
6	0.150	1.211	0.998	0.605	4.027	58.649
7	0.144	1.282	0.997	0.641	4.432	56.431
8	0.135	1.379	0.999	0.689	5.073	53.032

Table 3.2 Parameter Extraction of Contact Resistance, Sheet Resistance and Transfer Length

The R^2 value is known as the coefficient of determination which indicates the "goodness" of a fit for a particular set of data points. Values close to one indicate a very good fit of the data points. Once, the slope and y-intercept are obtained, all other parameters of interest can be calculated using the method described earlier. The average sheet resistance of the 10 nm Pt film was calculated to be 57 Ω/sq.

Figure 3.7 shows the total resistance versus distance curve for the 7 nm Pt sample for eight different TLM patterns. As can be seen in the figure, all eight TLM patterns except for one pattern (Pattern #2) exhibit linear behavior with a positive slope. The average sheet resistance of the 7 nm Pt film was calculated to be 103.9 Ω/sq.

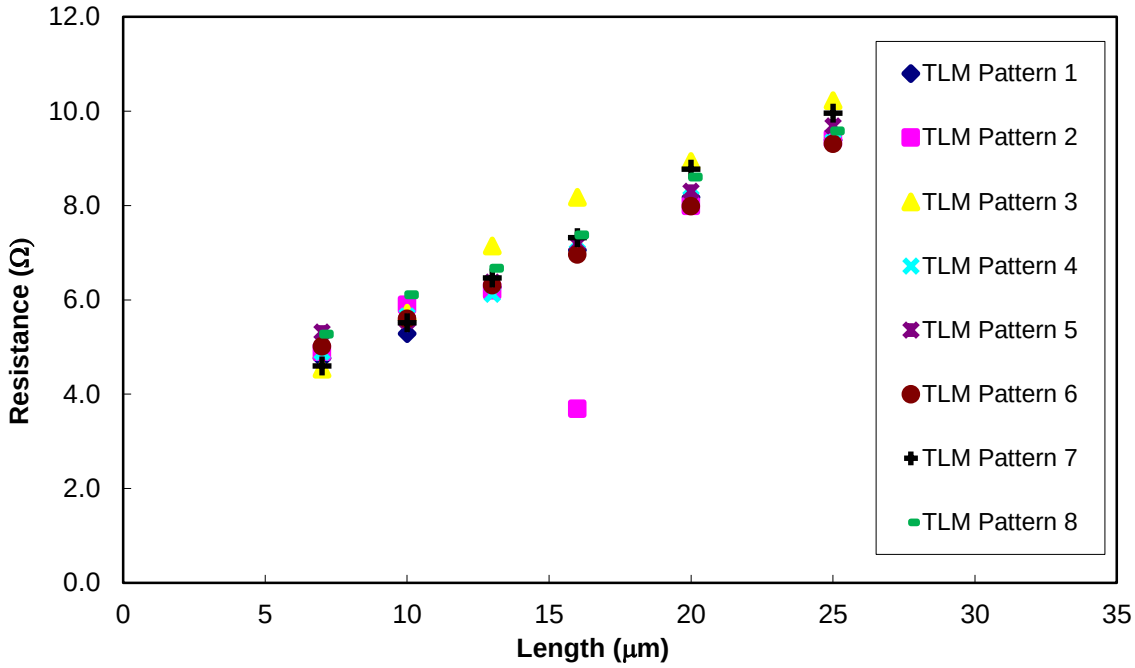

Figure 3.7 Total Resistance versus distance between the contacts for 7 nm Pt sample

Figure 3.8 shows the total resistance versus distance curve for the 10 nm Pt sample for eight different TLM patterns. As can be seen in the figure, all eight TLM patterns except

for one pattern (Pattern #8) show linear behavior with a positive slope. The average sheet resistance of the 13 nm Pt film was calculated to be 41.5 Ω/sq.

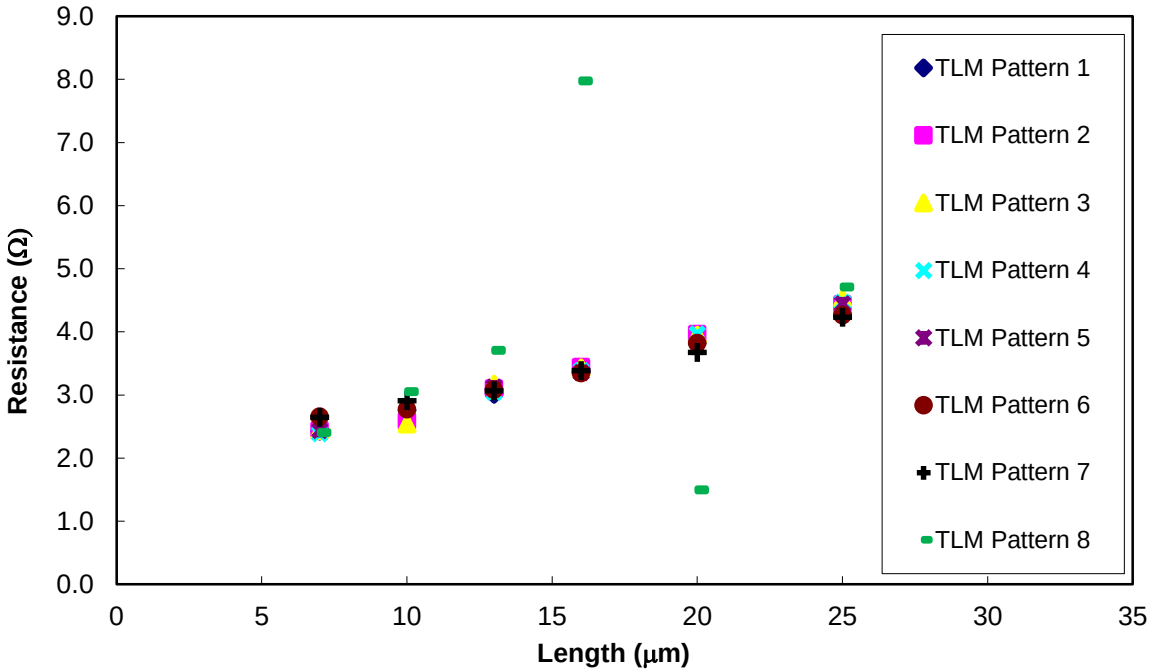

Figure 3.8 Total Resistance versus distance between the contacts for 13 nm Pt sample

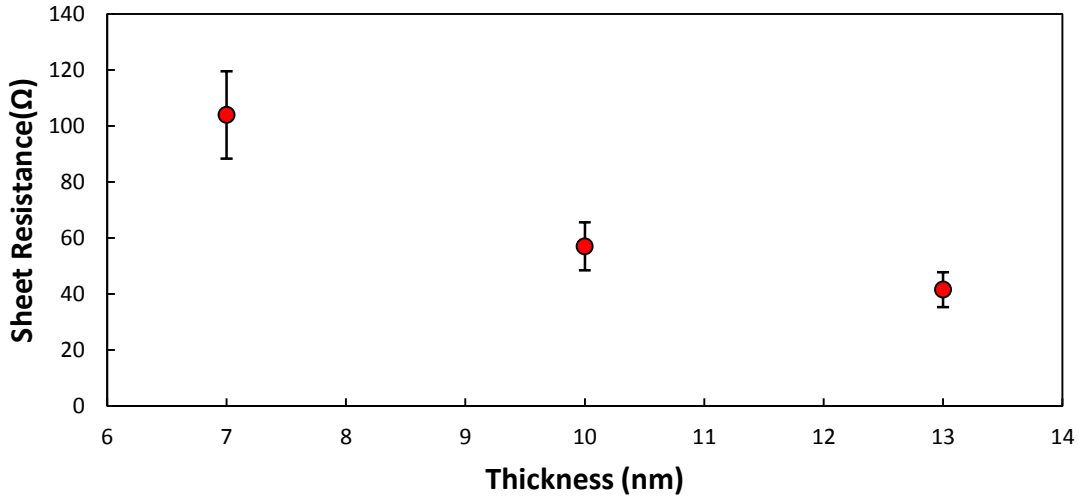

Figure 3.9 Sheet resistance as a function of Pt thickness

Figure 3.9 shows the average sheet resistance as a function of the thickness of platinum. It is evident from the figure that the sheet resistance of the Pt films decreases as the thickness of the Pt film increases, which is expected. The sheet resistance (R_{SH}) and the thickness of the metal film (t_F) can be used to calculate the resistivity (ρ) of the Pt film using the following equation.

$$\rho = R_{SH}.t_F \tag{3.20}$$

Table 3.3 shows calculated values of resistivity for the different thicknesses of Pt films.

Thickness of Pt film (nm)	**Resistivity (Ω.cm)**
7 nm	7.28e-5
10 nm	5.69e-5
13 nm	5.39e-5

Table 3.3 Resistivity of different thicknesses of Pt films

It is evident from *Table 3.3* that the resistivity of these thin films decreases as the thickness of the film increases. By definition, it is fair to assume that intrinsic properties of a metal film such as electrical resistivity should be independent of its thickness. However, this is not true for ultra-thin metal films. The resistivity of bulk Pt is 1.06e-5 Ω.cm. In the case of thin film metals, the resistivity is much larger than the resistivity of bulk metal; and it decreases with increasing thickness of the metal film, until it achieves a value close to the bulk resistivity. Moreover, the electrical resistivity of the metal film is affected by the film thickness as soon as the thickness of the film becomes comparable to the electron mean free path in that medium.

3.3.2 Optical Results

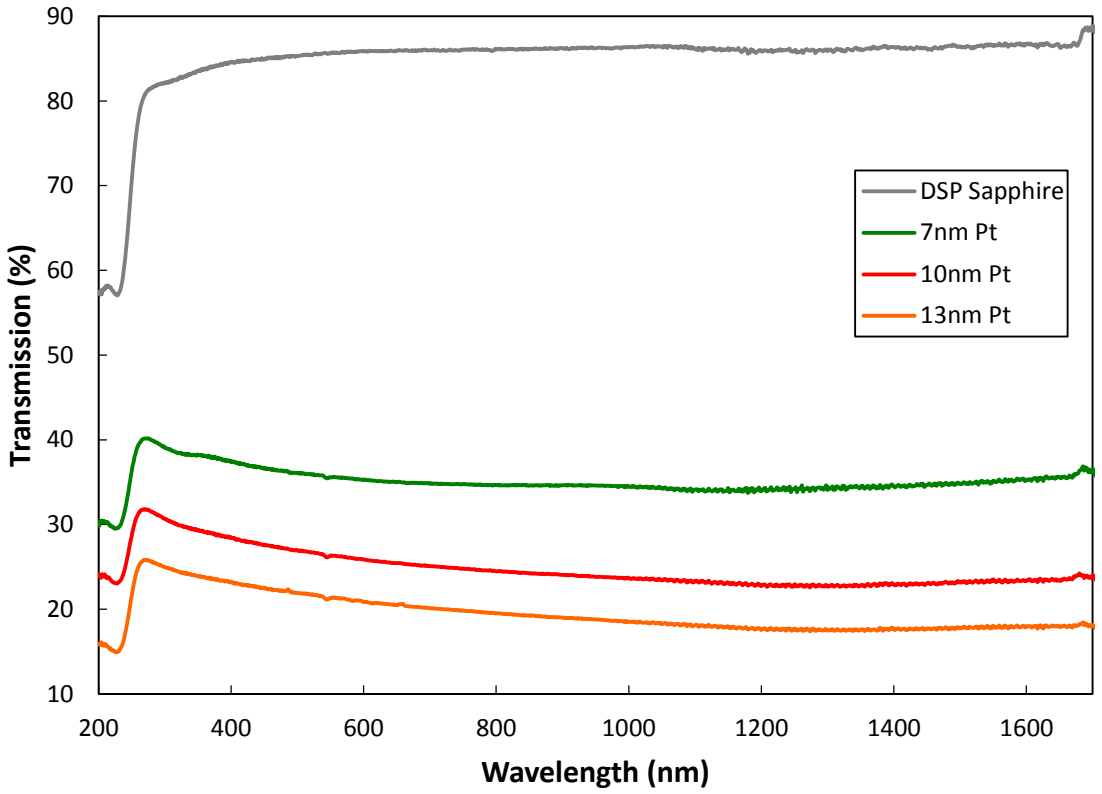

Figure 3.10 Transmission Spectra for 7 nm, 10 nm and 13 nm Pt films

Optical transmission measurements were made on Pt films with three different thicknesses (7 nm, 10 nm and 13 nm). These metal films were deposited in the same e-beam evaporation runs as the TLM samples described in *Section 3.3.1* (but the films were not patterned). *Figure 3.10* shows the raw transmission spectra. No effort has been made to correct these transmission spectra for reflection losses occurring at the air-Pt and Pt-Sapphire interfaces. It is evident in *Figure 3.10* that the overall transmission as a percentage decreases as the film thickness increases, which is expected.

3.3.3 Summary of Results

The measurement results shown herein demonstrate the connections between Pt film thickness, electrical sheet resistance and optical power transmission. While the sheet

resistance of the thin film decreases with increasing thickness, the optical transmission through the film increases with decreasing film thickness. Consequently, as suggested before, there is a tradeoff between the optical losses and series resistance for the transparent conductive films which will serve as key elements of the Schottky solar cells described next. An ideal transparent conductive film would yield the lowest possible values of optical loss and series resistance. However, from the results presented here, it is clear that both these properties cannot be achieved at the same time. Hence, an effective transparent conductive film needs careful optimization of both the electrical and optical properties in order to improve the performance of InGaN/GaN Schottky solar cells.

Chapter 4. Solar Cell Characterization

It is clear from the previous section that the thickness of the Pt films affect their electrical and optical properties. When a Pt film is used as a transparent conductive film in a Schottky solar cell, the optical properties of the Pt film influence the amount of light passing through it and reaching the absorber layer. On the other hand, the electrical resistivity of the Pt film impacts the collection of photo-generated carriers. As a result, the material properties of Pt (in thin-film form) should significantly impact the performance of the solar cell. Now that we have a better understanding of the Pt films and their properties; the next step is to understand the impact of film thickness on the photovoltaic properties of InGaN/GaN Schottky solar cells.

4.1 Solar Cell Structure

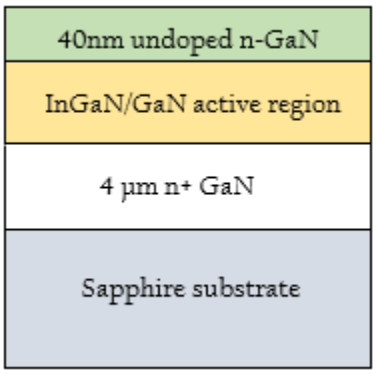

Figure 4.1 InGaN/GaN layer structure.

The InGaN/GaN structures were grown on c-plane sapphire substrates by organometallic vapor phase epitaxy (OMVPE). The layer structure grown is shown in *Figure 4.1*. The structure consists of a 4.0 μm thick, Si-doped n-GaN ohmic contact layer ($n = 2 \times 10^{18}$ cm^{-3}), followed by a nominally un-doped GaInN/GaN absorber capped by a 40 nm thick, un-

doped GaN window layer. The absorber consists of a 30-pair MQW region with 2.5 nm thick GaInN quantum wells and 12 nm thick GaN barriers. The indium content in the InGaN quantum wells is about 10%. Mesa fabrication was performed using an inductively coupled plasma (ICP) etching system to isolate devices from each other and also to expose the n-GaN ohmic contact layer. Pt is used as the transparent conducting film which also serves as a large-area Schottky contact to the un-doped GaN window layer. The Schottky metal films were deposited by electron-beam evaporation. Two distinct geometries, each having two different values of metal line pitch, are used as the top electrode. The first kind of geometry used is grid style geometry shown in *Figure 4.2*. The top-side metal traces are made of a Ni (50 nm) / Ag (400 nm) bilayer and have a line width of 5 μm.

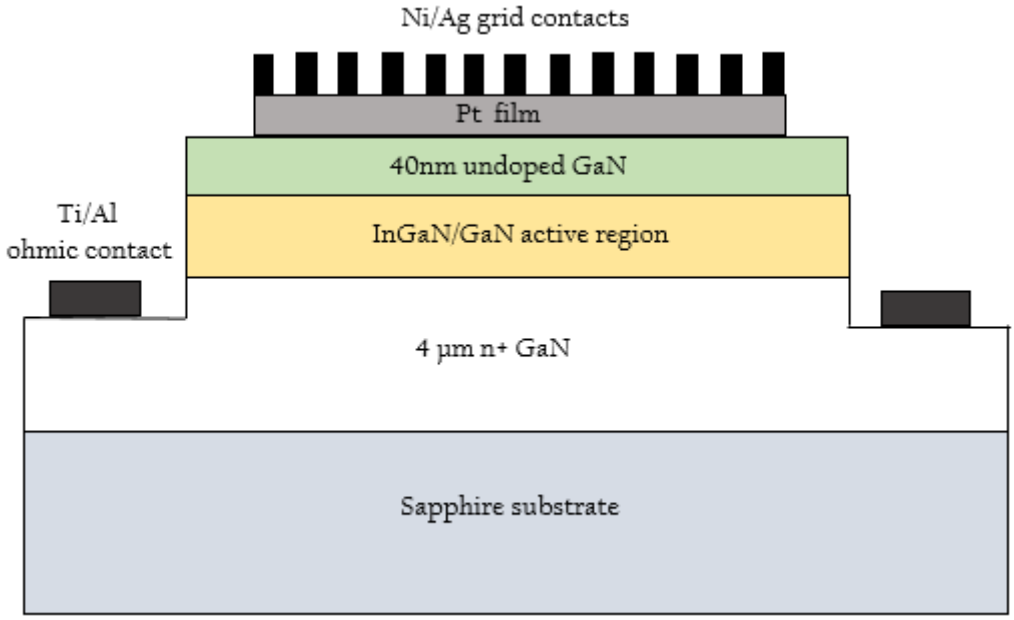

Figure 4.2 Cross-section of grid style InGaN solar cell

The device structure has a square-shaped mesa surrounded by another metal trace that serves as the bottom-side electrode. A Ti/Al (30nm/400nm) composite, deposited using electron beam evaporation, was used as the ohmic contact to n-type GaN. *Figure 4.3* shows

Nomarski optical images of fabricated solar cells with two different grid spacings (75 µm and 150 µm). The two contact patterns are referred to in the following discussion as coarse grid and fine grid.

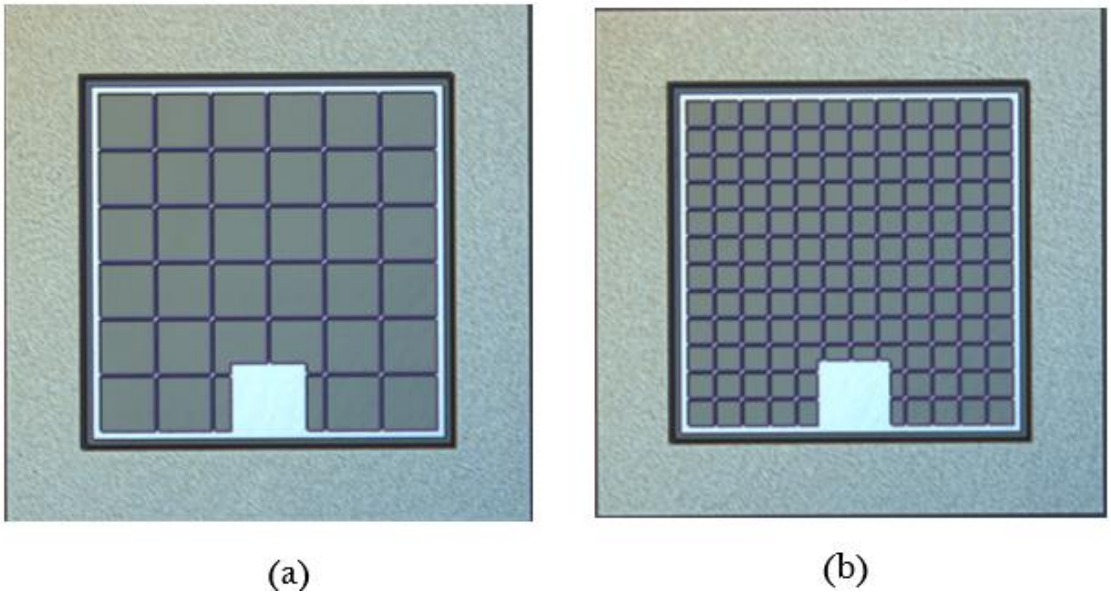

Figure 4.3 (a) Coarse Grid (b) Fine Grid

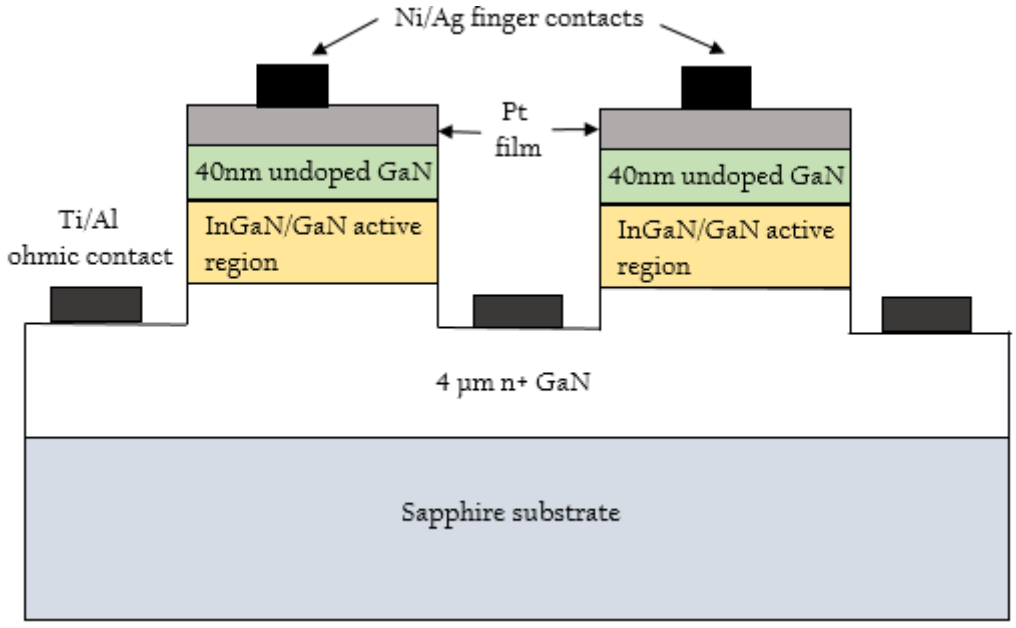

Figure 4.4 Cross-section of finger style InGaN solar cell

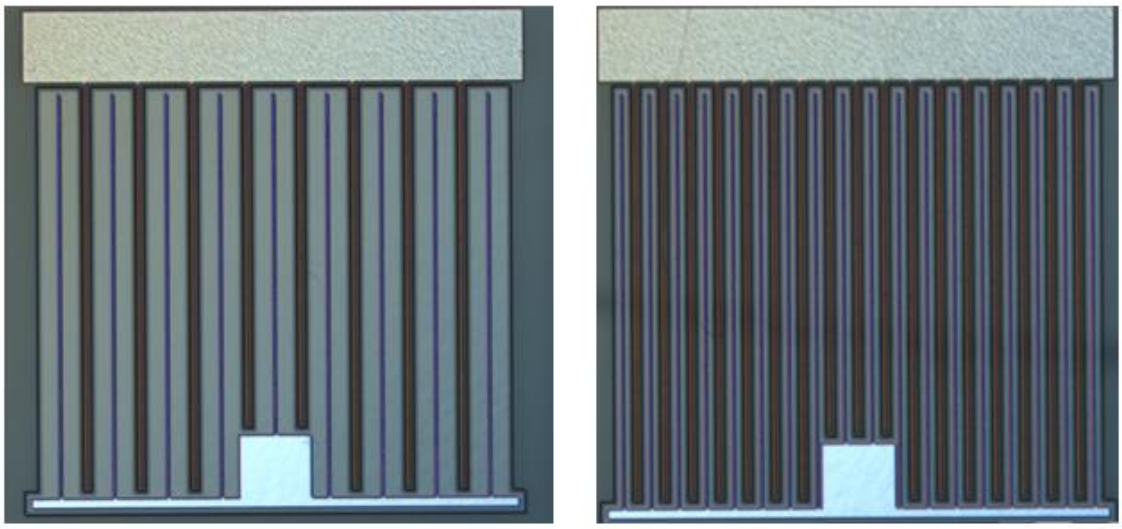

Figure 4.5 (a) Coarse Finger (b) Fine Finger

The second kind of electrode geometry used is a finger style geometry as shown in *Figure 4.4*. In this case, the mesa has an interleaved comb-like structure with the layer structure removed to make ohmic contact traces adjacent to each mesa finger. *Figure 4.5* shows fabricated solar cells with two different metal trace pitches (75 μm and 150 μm). These two contact patterns are referred to in the following discussion as coarse finger and fine finger.

Three different solar cells were fabricated using the same GaN/InGaN layer structure, each having the four different electrode geometries described above. Each solar cell had a different thickness of Pt, the thicknesses being 7 nm, 10 nm and 13 nm. The size of an entire solar cell device (including the non-mesa area) is 1.4 x 1.4 mm^2, and there is no anti-reflection coating for all four geometries.

4.2 Crosslight APSYS Simulation

Crosslight APSYS is a general-purpose software that uses the finite element method to simulate the performance of semiconductor devices. The program solves several equations simultaneously including the basic Poisson's equation and drift-diffusion current equations. Modelling InGaN based solar cells presents several challenges, the most important of which are uncertainty in key material parameters and proper implementation of spontaneous polarization and piezoelectric effects. Hence, in this work, GaN Schottky solar cells are investigated in order to avert these issues.

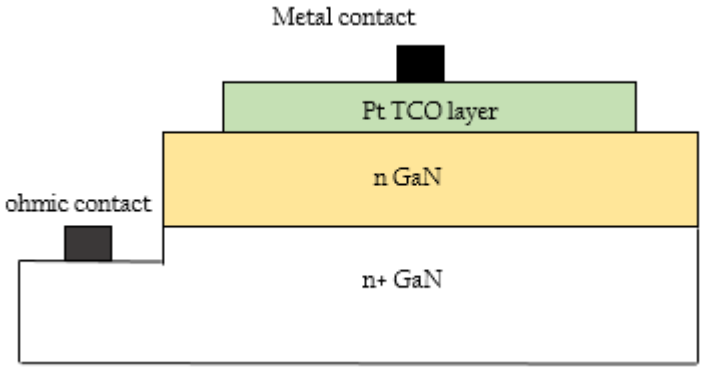

Figure 4.6 Schematic GaN Schottky Solar Cell

Simulations were used to study the impact of Pt layer thickness on short-circuit current density and open-circuit voltage of the solar cell. Only the coarse finger and fine finger geometries were used for simulation purposes. All physical dimensions used in the simulations match the actual solar cell devices in an effort to accurately model the 2D effects. *Figure 4.6* shows the schematic of the GaN solar cell simulated using Crosslight. The structure consists of a 2.0 μm thick n+ GaN ohmic contact layer ($n = 1 \times 10^{18}$ cm^{-3}), followed by a 0.5 μm thick n-type GaN ($n = 1 \times 10^{16}$ cm^{-3}) absorber layer. The thickness of the n-type GaN layer is equal to the thickness of the active region part of InGaN/GaN layer

structure. However, the thickness of the n+ GaN ohmic contact layer is 2 μm thinner than that of corresponding layer in the structure. However, this difference does not impact the short circuit current and open-circuit voltage values. Neither does it affect the trend that we observe for both the above mentioned parameters.

A thin film Pt layer is used to form a broad-area Schottky barrier to the n-GaN layer. However, the Pt layer does not cover the entire mesa surface; instead it is separated from the boundaries (of the n-GaN layer) by a distance of 10 μm on both sides. The two metal contacts, which are equidistant (60 μm) from the boundaries (of the GaN absorber layer) are 5 μm wide. An AM0 spectrum was used for illumination.

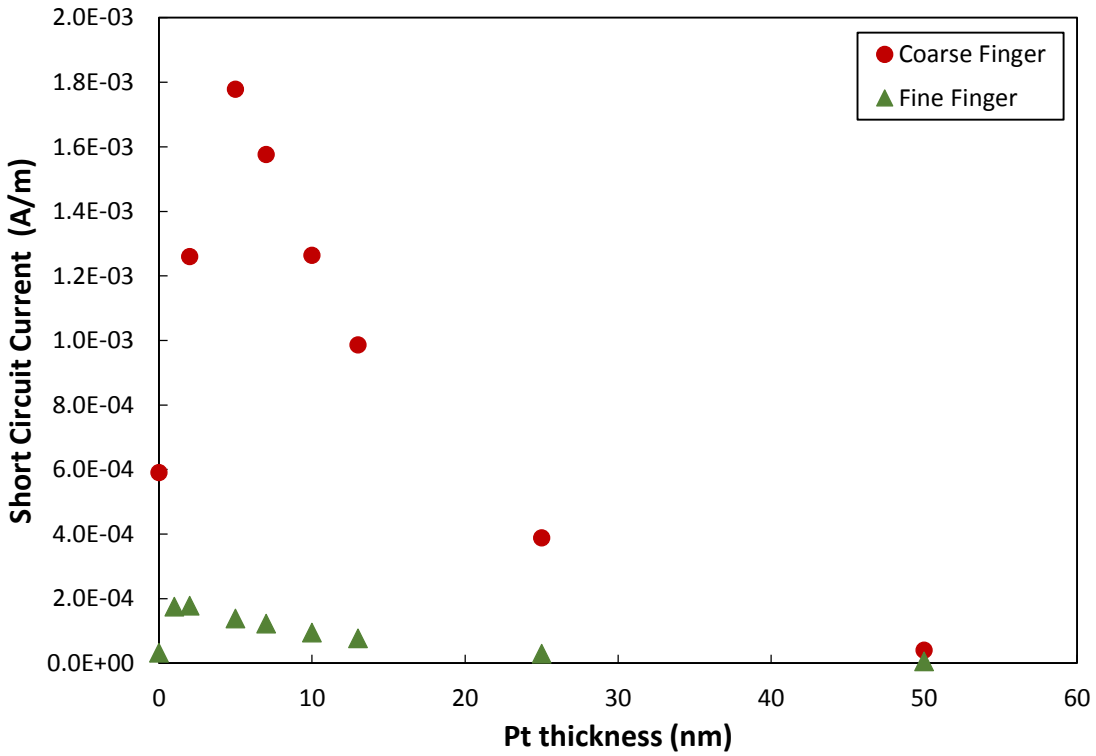

Figure 4.7 Short-circuit current per unit length vs Pt Thickness

Figure 4.7 shows a plot of the short-circuit current per unit length versus the thickness of the Pt layer. Current density vs. voltage (*J-V*) curves were obtained by dividing the calculated current per unit length by the illuminated device mesa width. The mesa width is 125 μm (50 μm) for the coarse (fine) finger case, but all other simulation parameters are held constant. *Figure 4.8* shows a plot of the short-circuit current density versus the thickness of the Pt layer.

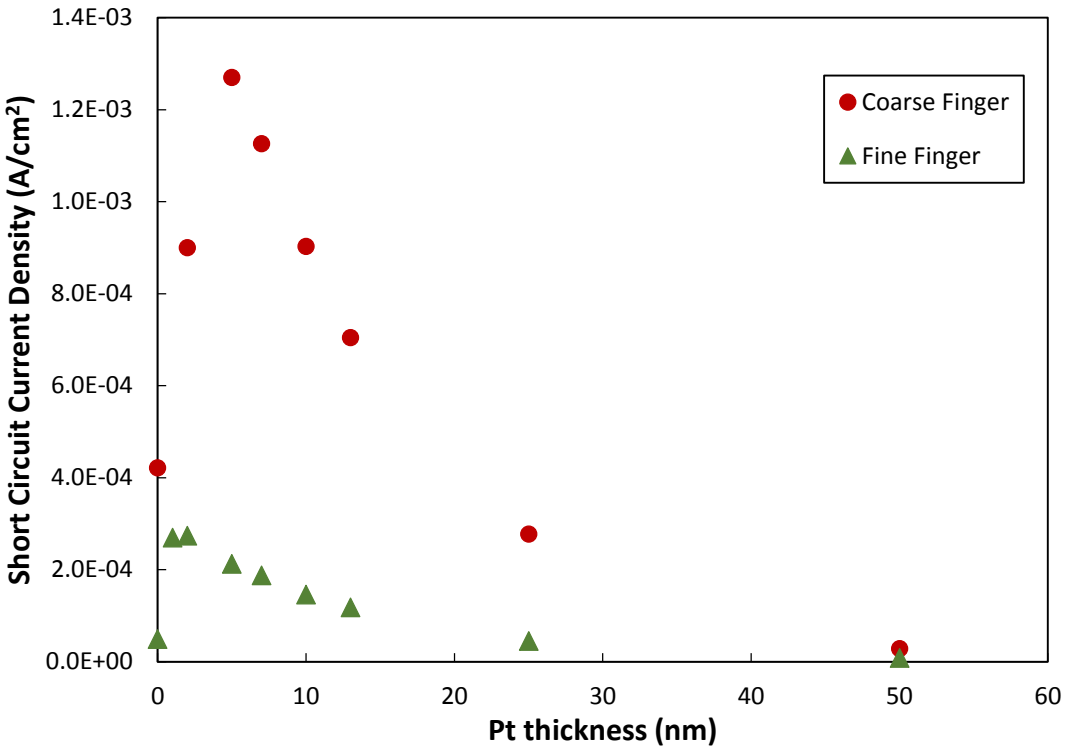

Figure 4.8 Short-circuit current density vs Pt Thickness

Figure 4.9 shows a zoomed-in plot of the short-circuit current density versus the thickness of the Pt layer. It is evident from *Figure 4.9* that J_{sc} is impacted by the thickness of the Pt layer. Moreover, the short-circuit current densities are larger for the coarse finger geometry as compared to the fine finger geometry.

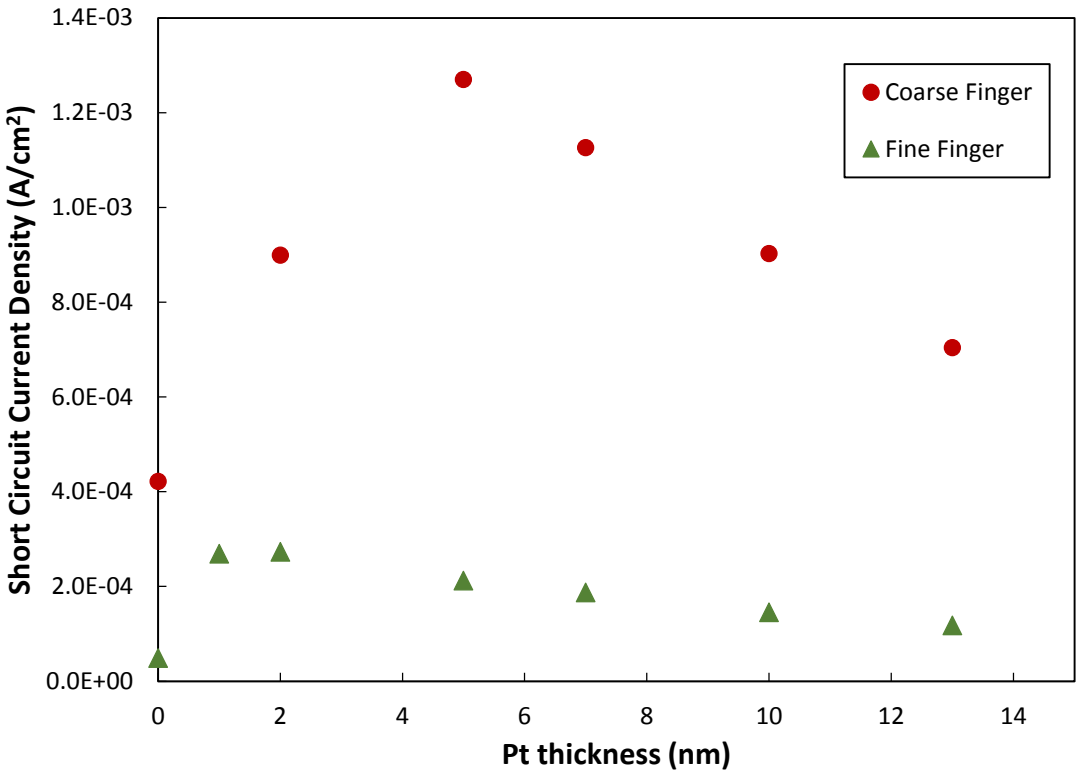

Figure 4.9 Short-circuit current density vs Pt Thickness (zoomed in)

The short-circuit current density is larger than in the reference case (i.e. no Pt film) for Pt layer thicknesses up to 15 nm (fine finger) or 50 nm (coarse finger). This observation justifies the need for a transparent conductive film. The short-circuit current density reaches a maximum value at roughly 2 nm and 5 nm for fine finger and coarse finger geometry, respectively. The presence of a maximum is explained by the balance of series resistance presented by the Pt layer and its optical losses. However, for thicknesses of the Pt layer greater than the aforementioned values for each geometry, there is a steady decrease in the short-circuit current density. This trend suggests that after a certain thickness, the short-circuit current density is impacted more by optical losses than by series resistance associated with the Pt layer.

Figure 4.10 shows a plot of the open-circuit voltage versus the thickness of the Pt layer. It is clear that the open-circuit voltage is only weakly affected by the change in the Pt layer thickness. The open-circuit voltage decreases by very small amounts with increasing Pt thickness. This trend can be explained by the logarithmic dependence of the open-circuit voltage on the short-circuit current (see *Equation 2.4*). Hence, the change in the thickness of the Pt layer affects the short-circuit current, which in turn affects the open-circuit voltage.

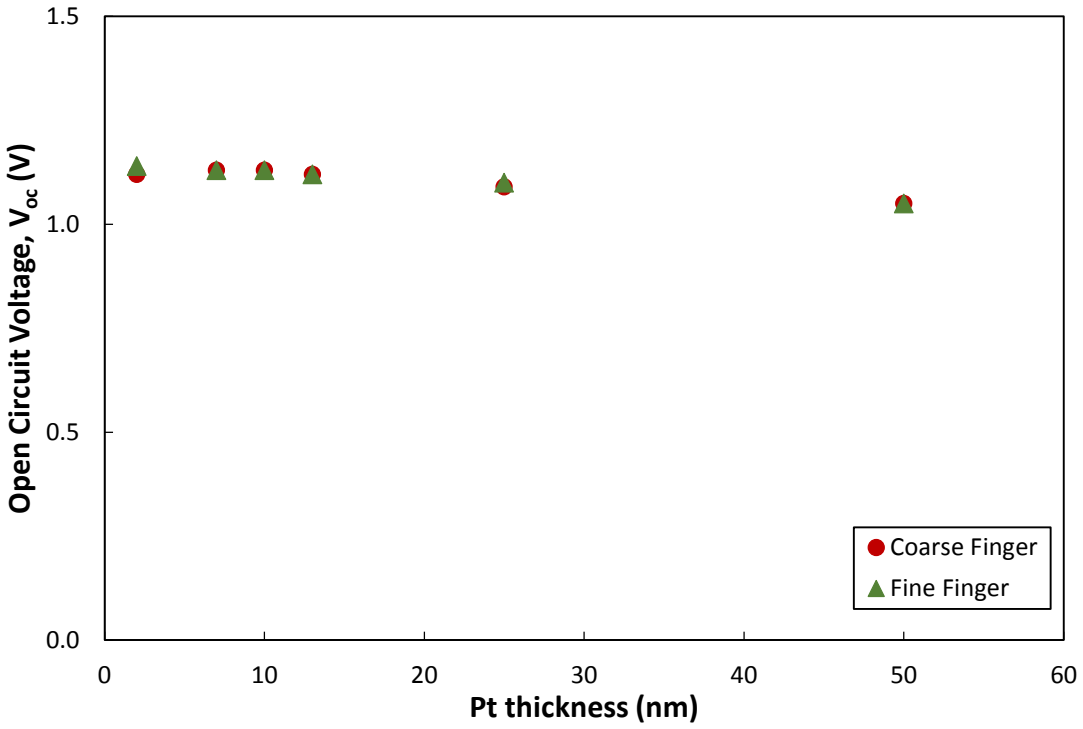

Figure 4.10 Open-circuit voltage vs Pt Thickness

In conclusion, computer simulations show that the use of a Pt layer increases the short-circuit current density for Pt film thicknesses less than 15 nm (fine finger) or 50 nm (coarse finger). Maximum short-circuit current density is achieved for a thickness of about 2 nm and 5 nm for the fine finger and coarse finger geometries, respectively. The open-circuit voltage is weakly affected by the change in the thickness of the Pt layer.

4.3 Characterization

4.3.1 Dark & Illuminated I-V Measurements

Fabricated solar cells have been characterized by current-voltage (I-V) measurements in the dark and under LED illumination at specific wavelengths. The three photon energies used for illumination are as follows: 3.5 eV ($E_{ph} > E_{g\ (GaN)}$), 3.15 eV ($E_{g\ (InGaN)} < E_{ph} < E_{g\ (GaN)}$) and 2.75 eV ($E_{ph} < E_{g\ (InGaN)}$). The power density of these LED sources were as follows: 100 $\mu W/cm^2$, 10 mW/cm^2 and 1 mW/cm^2 for 3.5 eV, 3.15 eV and 2.75 eV photon energies, respectively. These power densities were measured using a photo-detector connected to a Newport optical meter. Additional details regarding the measurement setup and calibration procedure can be found in *Appendix A.* Before, we analyze the results, it is important to understand the sources of error in our test methodology.

4.3.2 Sources of Error

This section deals with understanding possible sources of error in our test methodology used for electrical characterization of solar cells. A four-point measurement configuration is used to contact the solar cell for I-V characterization. This approach is preferred over a two-point measurement configuration because of accuracy concerns. In a two-point probe case, the current is sourced and the voltage is measured using the same set of probes. Since the same probes are used for both operations, the voltage drop across the wires and probes contribute to the voltage measured by the voltmeter. The use of another set of probes to measure the voltage separately using a high-impedance voltmeter gives more accurate results as it only measures the voltage across the device under test (DUT).

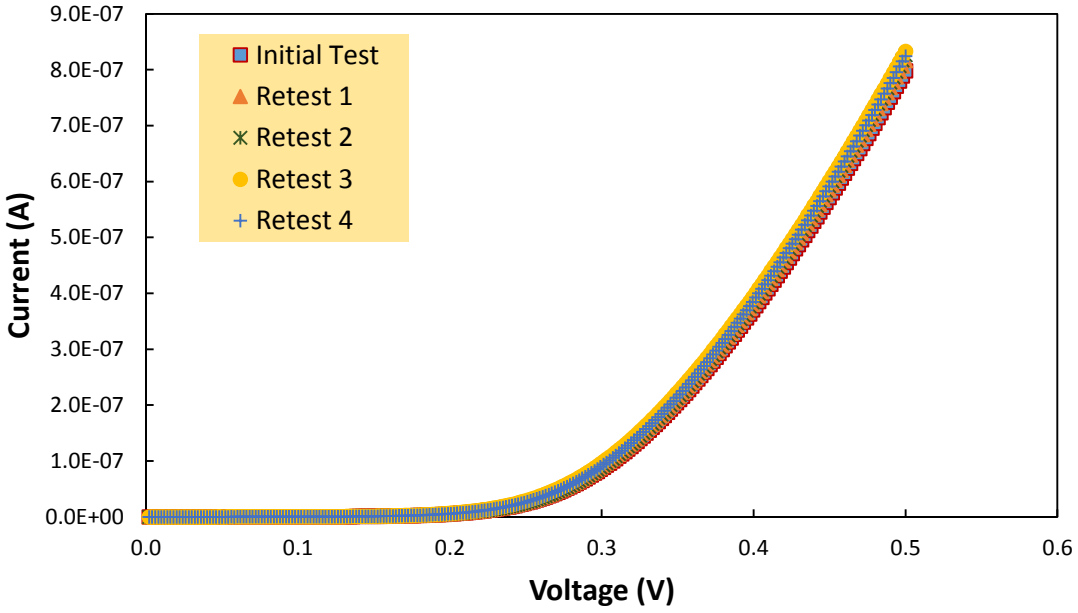

Figure 4.11 I-V curves of a solar cell in the dark

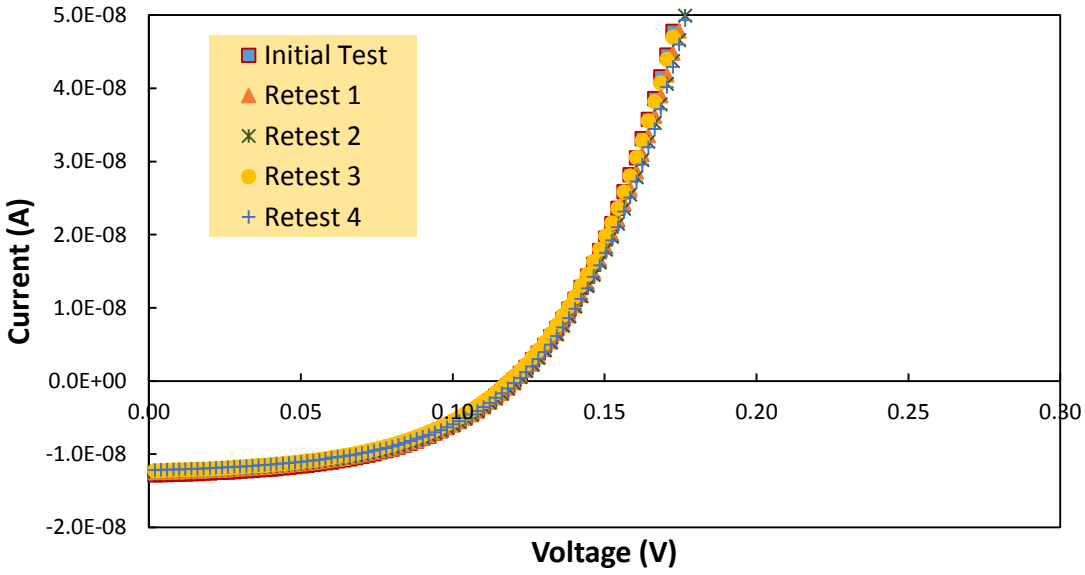

Figure 4.12 I-V curves for the same solar cell under illumination

I-V measurements are subject to a number of errors which must be accounted for. Few errors arise because experimental conditions change with every measurement. The possible

sources of error include variations in electrical probe positioning and pressure applied to them, non-uniformity of the light beam from the light source, temperature change, external noise and errors introduced due to the electronic instruments. In order to understand the impact of these variations, one of the solar cell devices was measured multiple times under dark and illuminated conditions. The dark and illuminated I-V plots are shown in *Figure 4.11* and *Figure 4.12*. The overlapping of all the I-V curves for both cases demonstrate good measurement reproducibility.

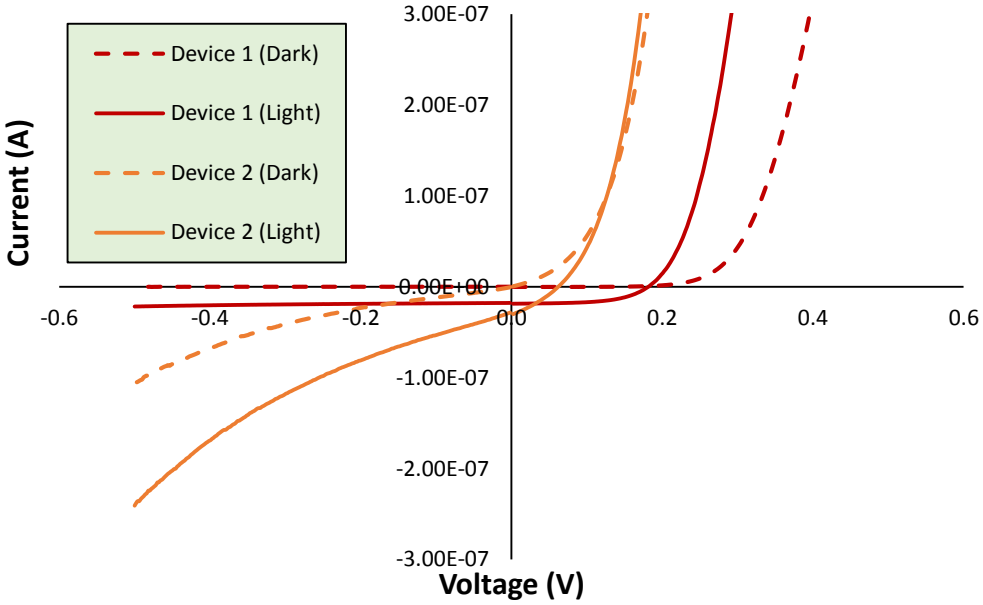

Figure 4.13 I-V curves of solar cells under dark and illuminated conditions

Another source of error in evaluating solar cell performance is low yield after device fabrication. An attempt was made to reduce the consequences of low fabrication yield by inspecting the processed wafer under a Nomarski-contrast optical microscope in order to eliminate devices with visible defects from the measurement set. Moreover, devices that exhibited large reverse (leakage) currents at small negative bias voltages were also eliminated from the analysis. Such “leaky diodes” were discarded because of their unusual

behavior when tested as solar cells under LED illumination. It can be seen in *Figure 4.13* that 'Device 2', which is one such leaky device has higher short-circuit current, lower open circuit voltage and a smaller fill-factor compared to 'Device 1' (normal solar cell).

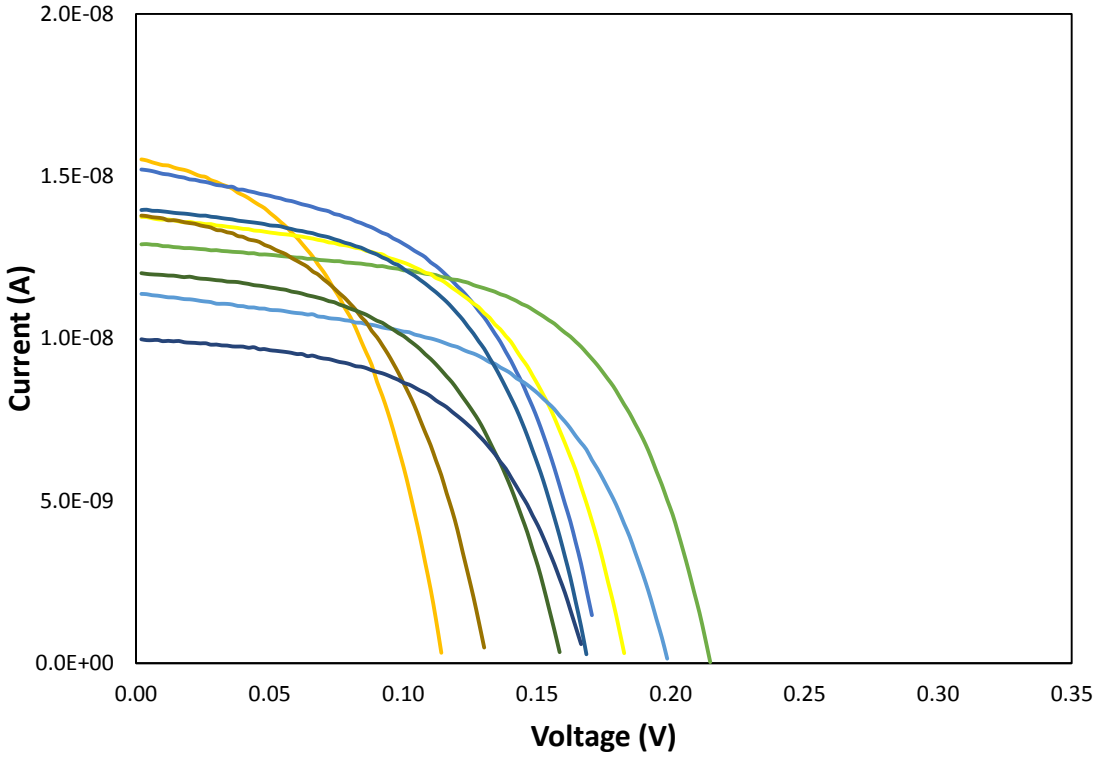

Figure 4.14 I-V curves for different InGaN/GaN-Pt solar cell devices under 395 nm LED illumination

Even after the initial device screening described above, considerable variability remains in the measured I-V arises for "good" solar cells distributed across the processed sample (1 x 1 cm^2). *Figure 4.14* shows current-voltage (I-V) curves for eight different solar cell devices on the 10 nm Pt-InGaN/GaN solar cell sample under 395 nm LED illumination at room temperature. This wavelength corresponds to a photon energy of 3.15 eV which will be absorbed by the InGaN layers in the solar cell but not by the GaN layers. I-V curves having leaky behavior or visible fabrication errors have already been eliminated from the consideration.

It is observed that different devices on the same sample give different photo-response. However, some of the variation can be explained by the fact that devices that have lower short-circuit current have a reduced open-circuit voltage (see *Equation 2.4*). But, this observation is not true for all device measured. Hence, in order to understand the variation, same devices were illuminated with LEDs having a wavelength of 355 nm. This wavelength corresponds to a photon energy of 3.5 eV which should be absorbed by both GaN and InGaN layers within the material structure. *Figure 4.15* shows I-V curves for the same eight solar cells under 355nm LED illumination at room temperature.

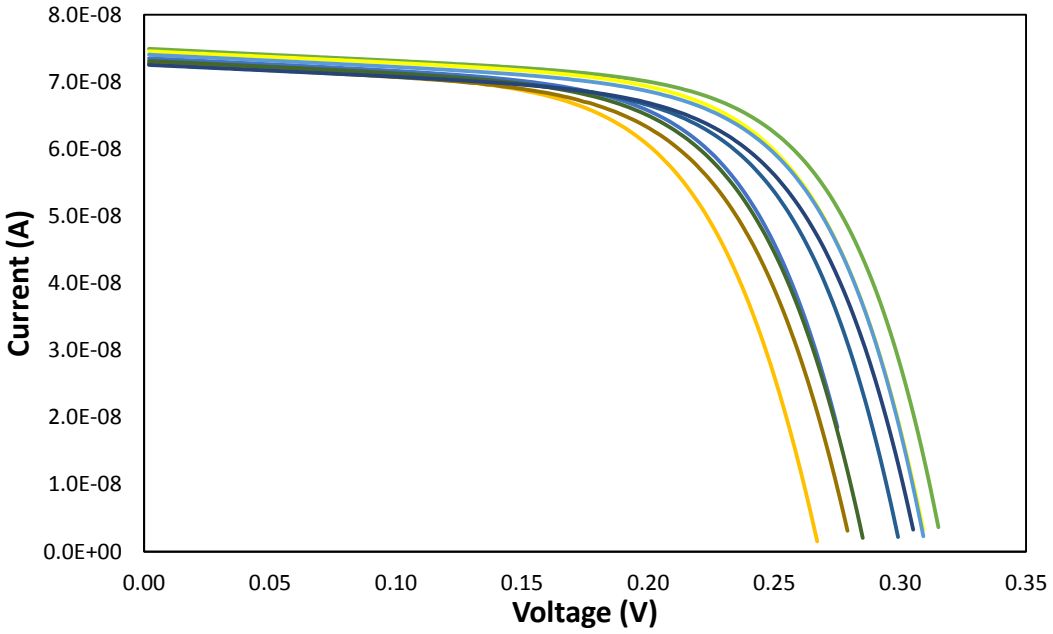

Figure 4.15 I-V curves for different InGaN/GaN-Pt solar cell devices under 355 nm LED illumination

With the 355 nm LED illumination, the short-circuit current was more consistent for different devices compared to the open circuit voltage values. Variability observed for the open-circuit voltage values may be attributable to inhomogeneity of barrier heights formed across the sample. However, this is just speculation. It could well be some second-order effect occurring at the metal-GaN interface which needs further investigation. One possible

explanation for this behavior is inhomogeneity in the quality of the InGaN absorber layer. *Table 4.1* shows average values of short-circuit current and open-circuit voltage, along with the associated standard deviations for both 395 nm and 355 nm LED illumination.

	Average value	**Standard Deviation**
I_{sc} (395 nm LED)	13.2 nA	1.7 nA (± 12.8%)
I_{sc} (355 nm LED)	73.4 nA	0.8 nA (± 1.1%)
V_{oc} (395 nm LED)	169 mV	29 mV (± 17.1%)
V_{oc} (355 nm LED)	297 mV	15 mV (± 5.1%)

Table 4.1 Average short-circuit current and open circuit voltage values along with standard deviation

It is evident from *Table 4.1* that the standard deviations for both J_{sc} and V_{oc} are almost 2x larger for 395 nm LED illumination as compared to 355 nm LED illumination.

4.4 Experimental Results

With confidence established in our characterization techniques, and all possible sources of error identified, we can now proceed to analyze trends in solar cell performance in relation to the changes in the Pt layer thickness and device geometry. *Figure 4.16*, *Figure 4.17*, *Figure 4.18* and *Figure 4.19* show the measured current-voltage (I-V) characteristics of solar cells (with different geometries) with a 7 nm, 10 nm and 13 nm Pt metal film used as the transparent conductive film under 395nm LED illumination at room temperature. It is evident from *Figure 4.16* and *Figure 4.17* (for both grid style geometries) that the highest short-circuit current is exhibited by the solar cell with a 10 nm Pt transparent conductive film. But, the highest open-circuit voltage is exhibited by the solar cell with the 13 nm Pt film.

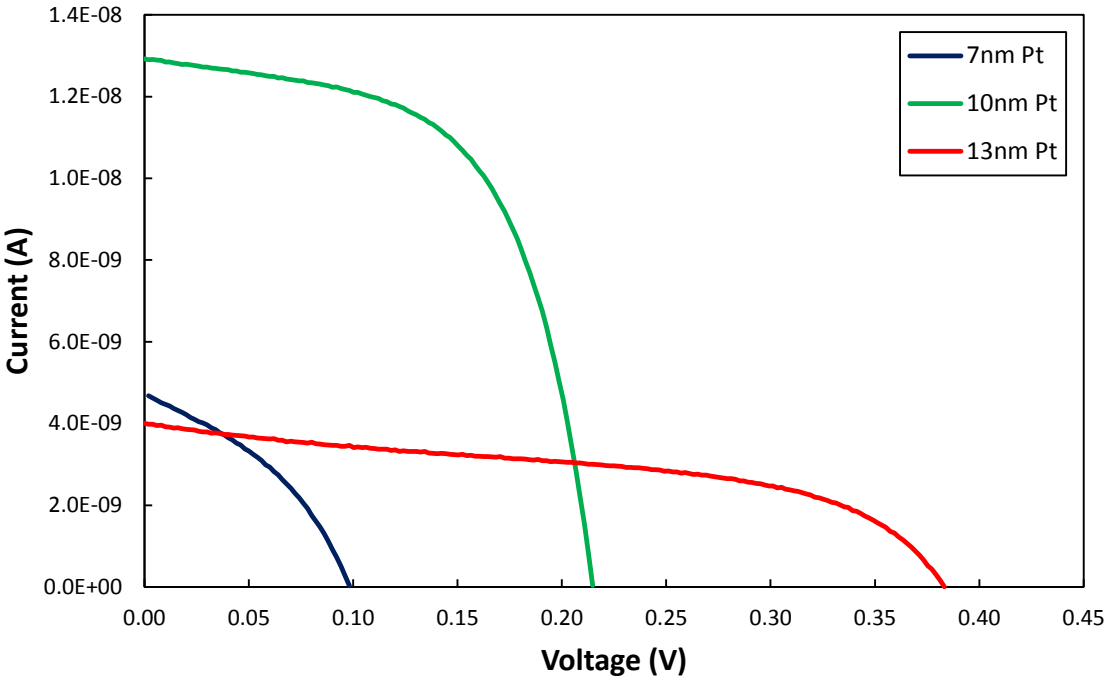

Figure 4.16 I-V curves of InGaN/GaN-Pt coarse grid solar cell devices under 395 nm LED illumination

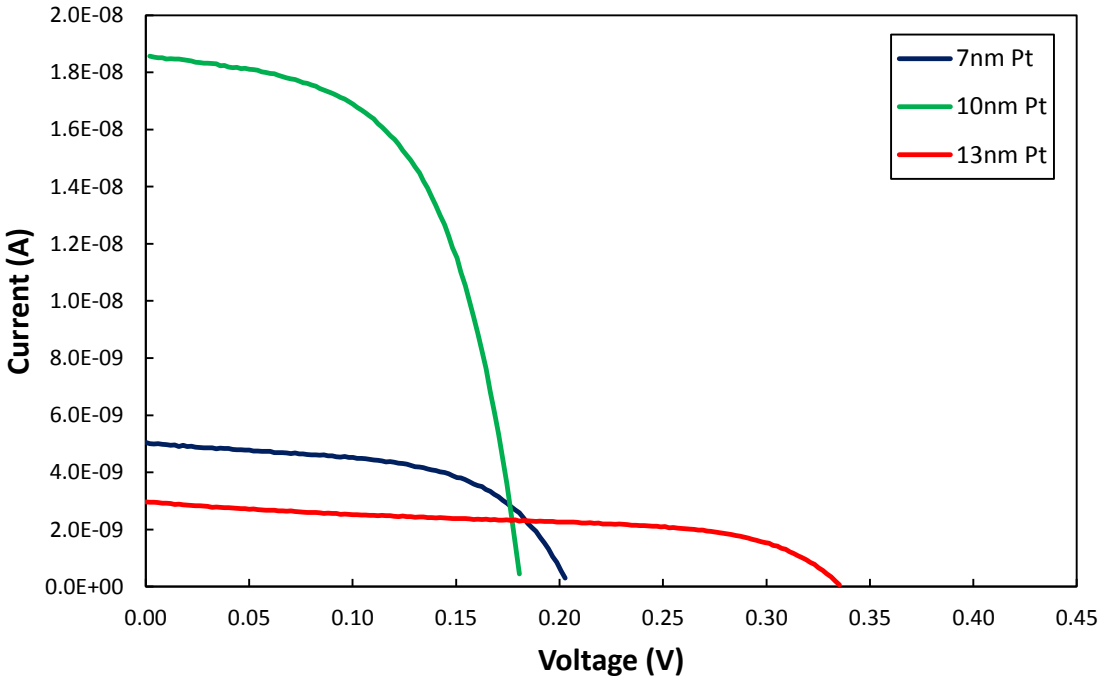

Figure 4.17 I-V curves of InGaN/GaN-Pt fine grid solar cell devices under 395 nm LED illumination

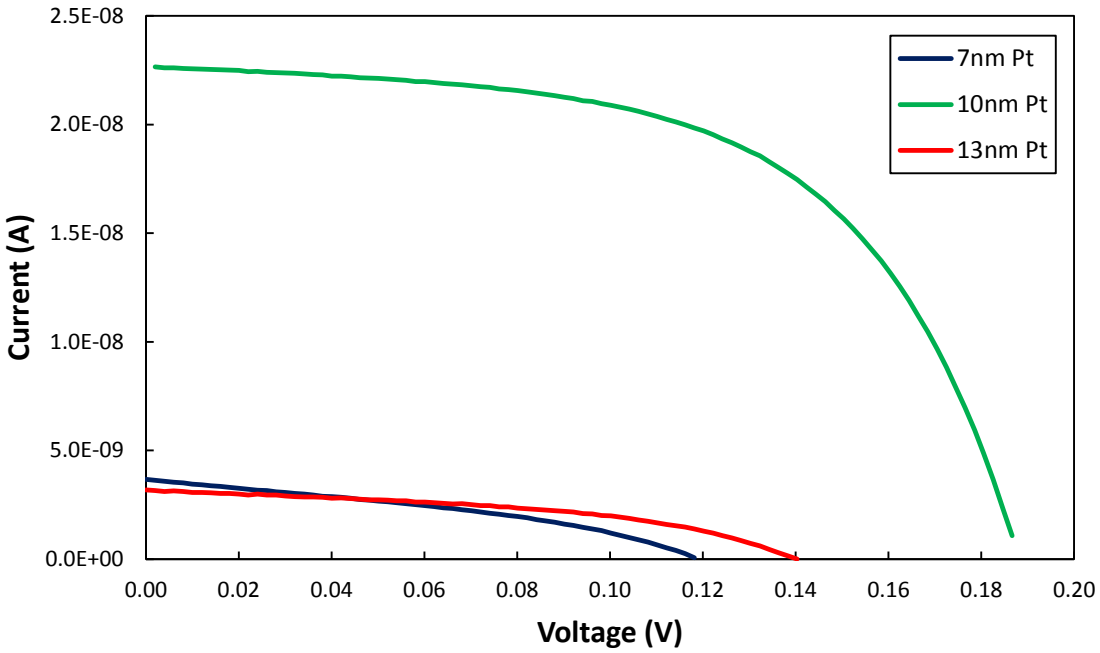

Figure 4.18 I-V curves of InGaN/GaN-Pt coarse finger solar cell devices under 395 nm LED illumination

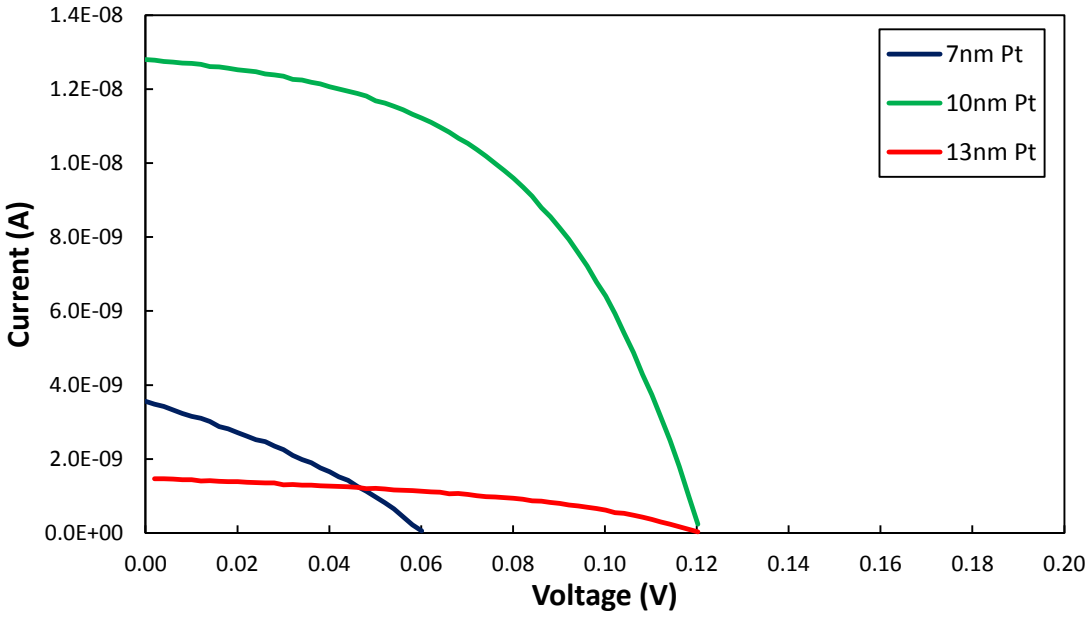

Figure 4.19 I-V curves of InGaN/GaN-Pt fine finger solar cell devices under 395 nm LED illumination

In the case of both finger-style geometries, it is evident from *Figure 4.18* and *Figure 4.19* that the highest short-circuit current and open-circuit voltage are exhibited by the solar cell with the 10 nm Pt film. Hence, it can be concluded that the highest short-circuit current is exhibited (for all four different geometries) by the solar cell with a 10 nm Pt film. *Figure 4.20* shows the measured current-voltage (I-V) characteristics of solar cells (with different geometries) with a 10 nm Pt film used as the transparent conductive film under 395nm LED illumination at room temperature.

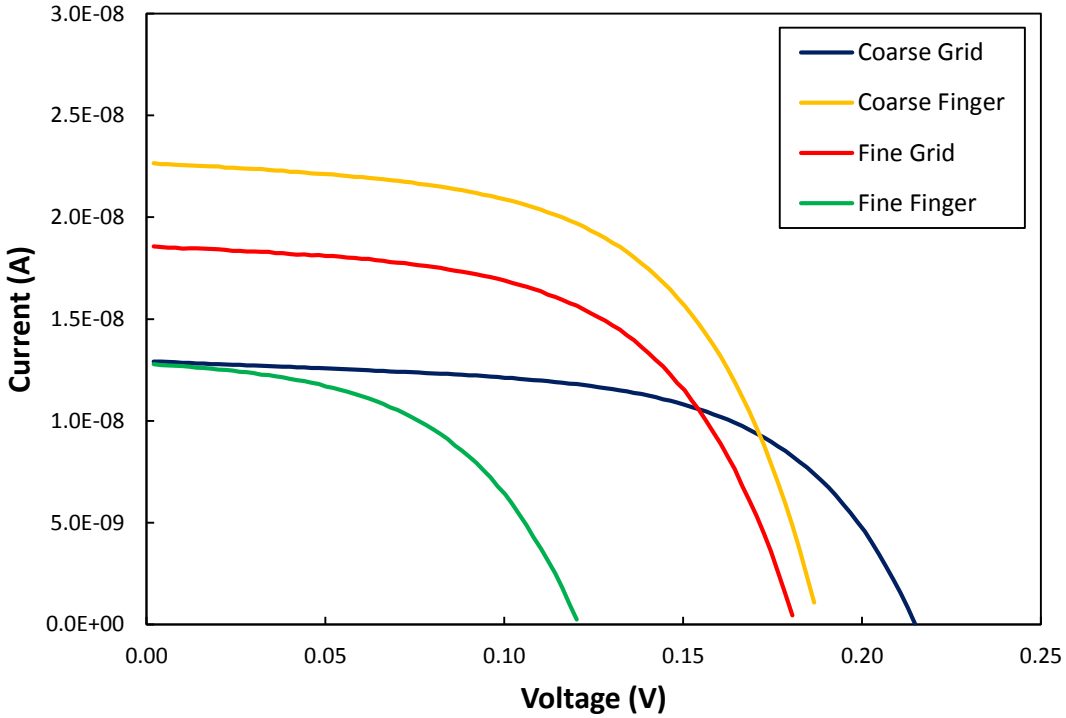

Figure 4.20 I-V curves of InGaN/GaN-Pt (10 nm) solar cell devices under 395 nm LED illumination

Considering the different electrode geometries, there are two important parameters that affect the short-circuit current density. The two parameters are shading losses due to the area occupied by the opaque Ni/Ag contacts pads, and surface recombination. Key differences in the finger and grid patterns are best illustrated by referring to *Table 4.2*.

	Mesa Area (cm^2)	***Illuminated Area (cm^2)***	***Bulk Volume (cm^3)***
Coarse Grid	*0.009604*	*0.008083*	*4.17E-7*
Fine Grid	*0.009604*	*0.007594*	*4.17E-7*
Coarse Finger	*0.013591*	*0.012404*	*5.91E-7*
Fine Finger	*0.011088*	*0.009403*	*4.82E-7*

Table 4.2 Key differences in finger and grid patterns

Moreover, the perimeter of the mesa area for the finger patterns is larger compared to the grid patterns. A larger perimeter results in more dangling bonds present at the surface which act as recombination centers for minority carriers as explained previously in *Section 2.1*. As a result, there should be a higher probability of surface recombination in the two finger geometries which will result in a smaller short-circuit current. High recombination probability increases the forward diffusion current which also reduces the open-circuit voltage. Apart from surface recombination, shading losses due to the opaque Ni/Ag contact pads reduce the short circuit current. The four electrode geometries in decreasing order of their respective illuminated areas are: Coarse Finger, Coarse Grid, Fine Finger and Fine Grid. Another parameter that weakly affects the short-circuit current and open-circuit voltage is series resistance of the contact pads.

Figure 4.20 shows the measured current-voltage (I-V) characteristics of solar cells (with different geometries) with a 10 nm Pt film used as the transparent conductive film under AM 1.5 spectrum illumination at room temperature. However, the sample used for the above mentioned measurement has a different layer structure than the one mentioned

before. This particular sample had a layer structure which had 15 pairs of MQW (multi-quantum well) region unlike the previous sample which had 30 pairs of MQW region.

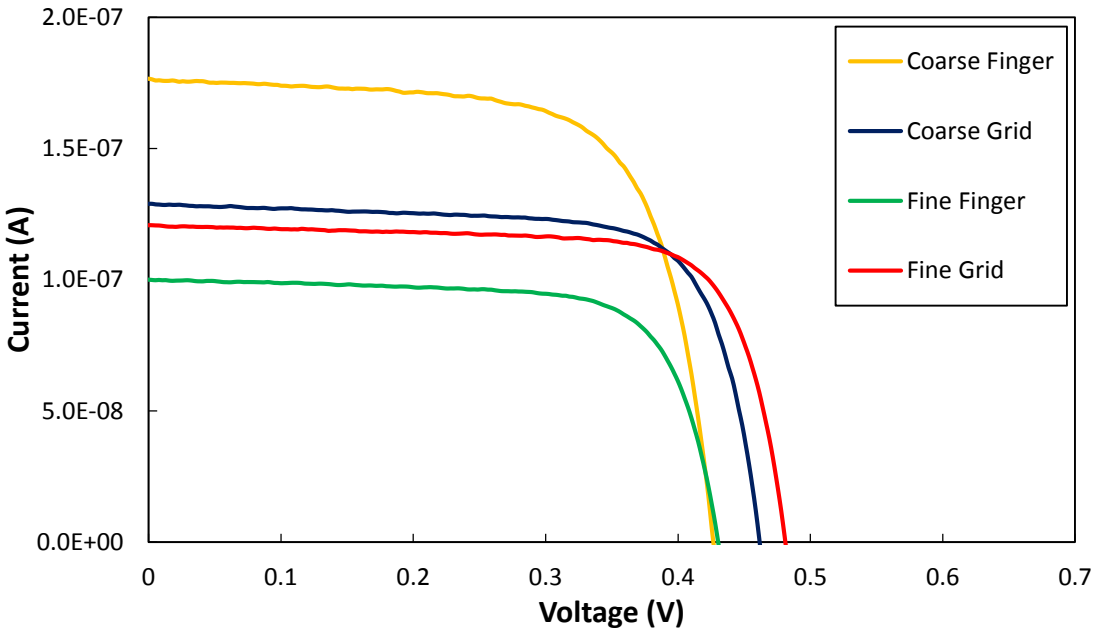

Figure 4.21 I-V curves of InGaN/GaN-Pt solar cell devices under AM 1.5 illumination

4.5 Data Analysis and Discussion

Figure 4.22, Figure 4.23, Figure 4.24 and Figure 4.25 show the calculated current density-voltage (J-V) characteristics of solar cells (with different geometries) with a 7 nm, 10 nm and 13 nm Pt metal film used as the transparent conductive film under 395nm LED illumination at room temperature. Current density vs. voltage (J-V) curves were obtained by dividing the measured current by the illuminated device mesa area. No attempt was made to correct for optical losses associated with reflection off the device surface. It is evident from *Figure 4.22* and *Figure 4.23* (for both grid style geometries) that the highest short-circuit current density is exhibited by the solar cell with a 10 nm Pt transparent

conductive film. But, the highest open-circuit voltage is exhibited by the solar cell with the 13 nm Pt film as noted previously.

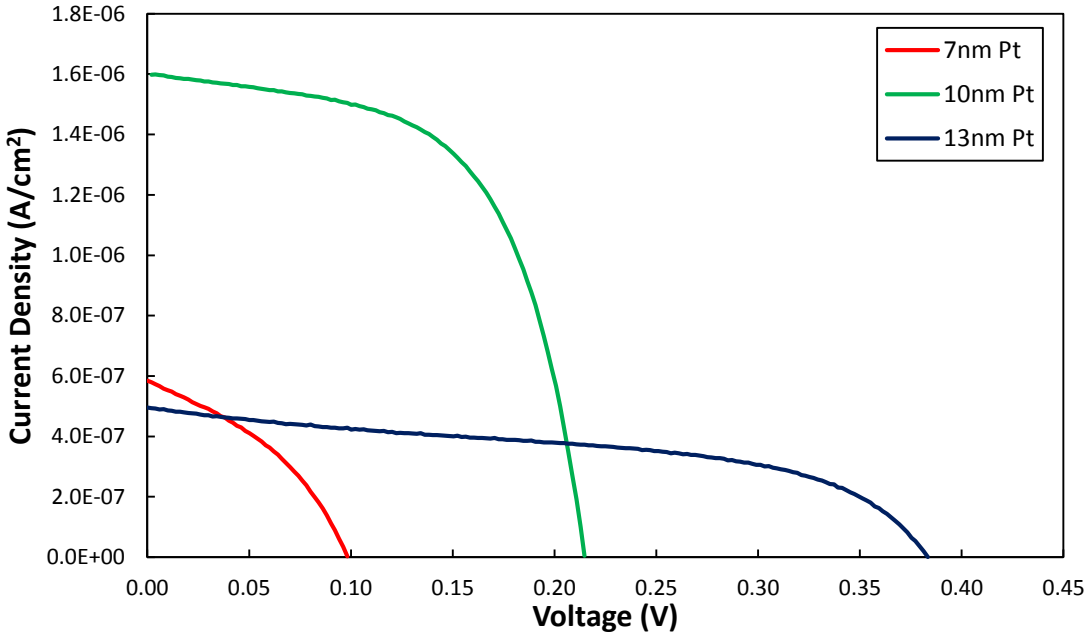

Figure 4.22 J-V curves of InGaN/GaN-Pt coarse grid solar cell devices under 395 nm LED illumination

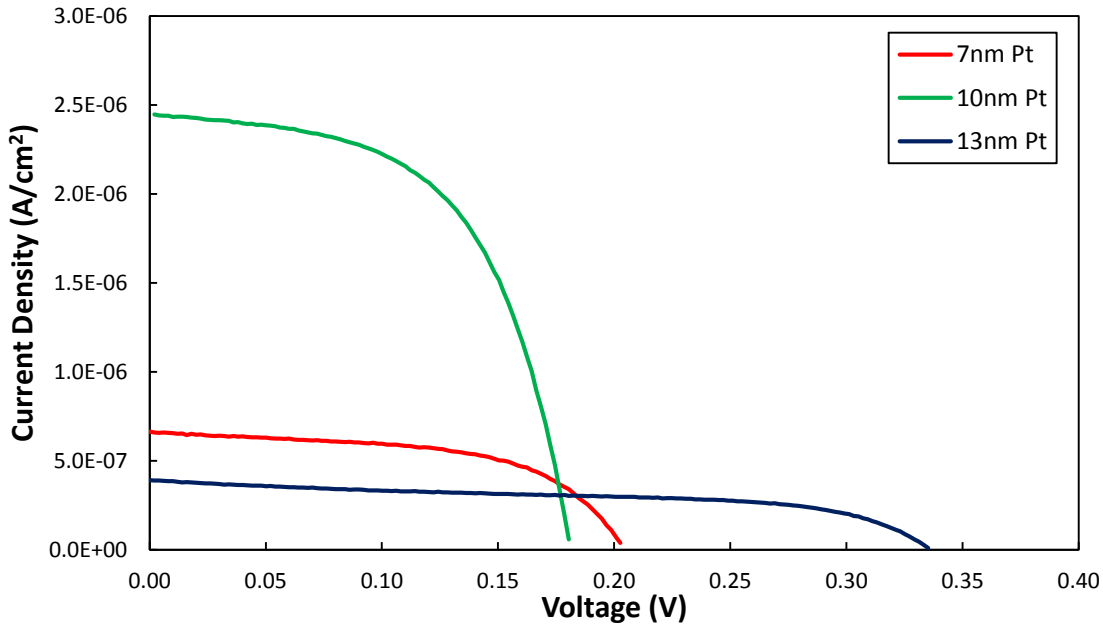

Figure 4.23 J-V curves of InGaN/GaN-Pt fine grid solar cell devices under 395 nm LED illumination

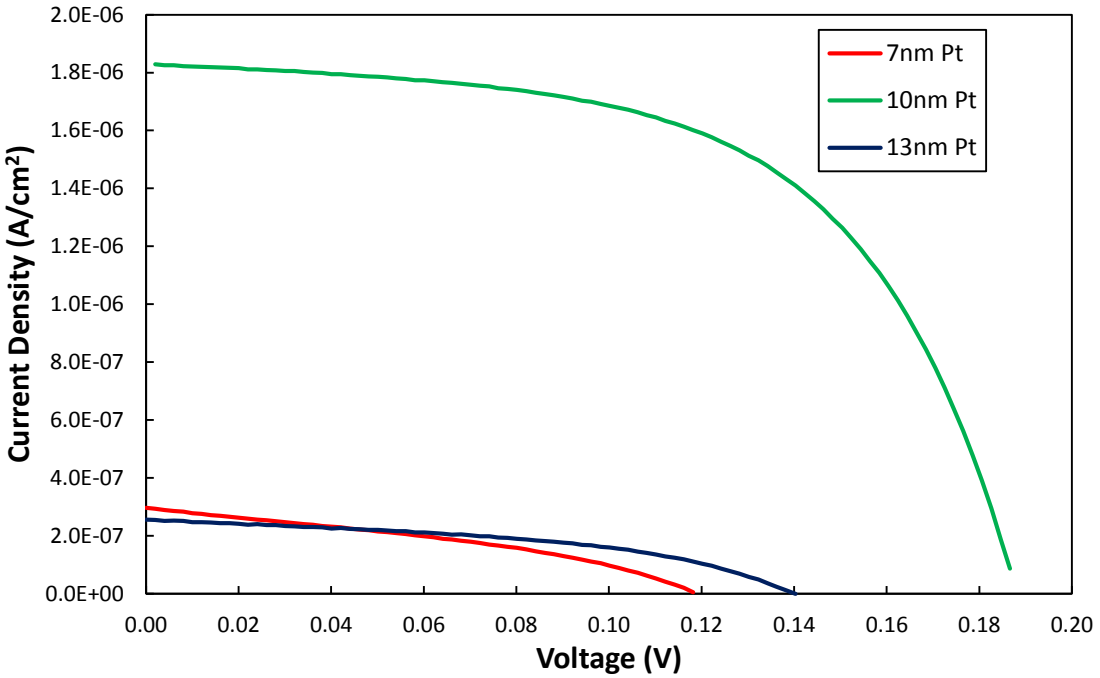

Figure 4.24 J-V curves of InGaN/GaN-Pt coarse finger solar cell devices under 395 nm LED illumination

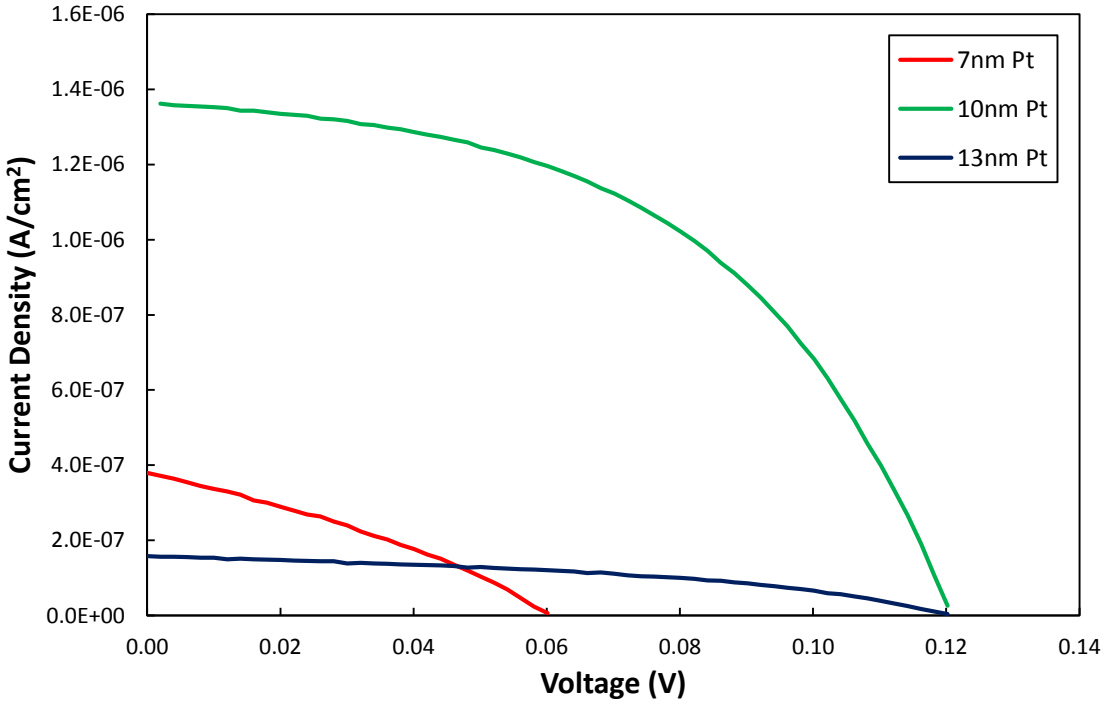

Figure 4.25 J-V curves of InGaN/GaN-Pt fine finger solar cell devices under 395 nm LED illumination

It is evident from *Figure 4.24* and *Figure 4.25* that the highest short-circuit current density and open-circuit voltage are exhibited by the solar cell with the 10 nm Pt film. Hence, it can be concluded that the highest short-circuit current density is exhibited (for all four different geometries) by the solar cell with a 10 nm Pt film. *Figure 4.26* shows the measured current density-voltage (J-V) characteristics of solar cells (with different geometries) with a 10 nm Pt film used as the transparent conductive film under 395nm LED illumination at room temperature.

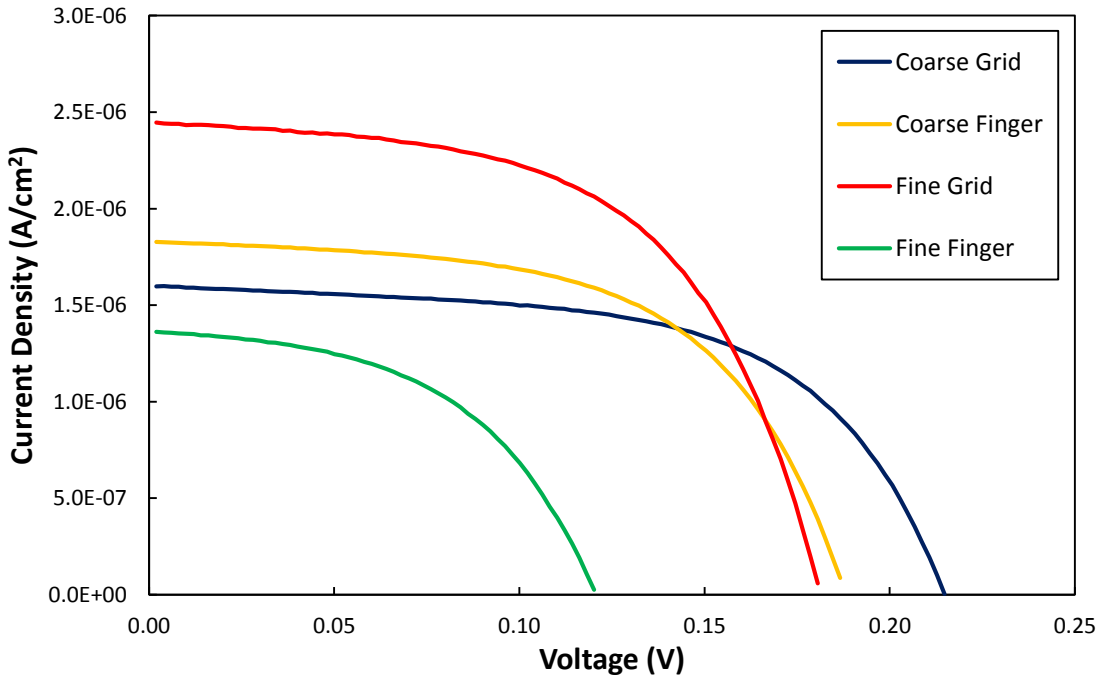

Figure 4.26 J-V curve of InGaN/GaN-Pt (10 nm) solar cell devices under 395 nm LED illumination

Figure 4.27 shows the measured current density-voltage (J-V) characteristics of solar cells (with different geometries) with a 10 nm Pt film used as the transparent conductive film under AM 1.5 spectrum illumination at room temperature. As noted before, the above mentioned measurements were made on a sample with a different layer structure (explained previously in this section).

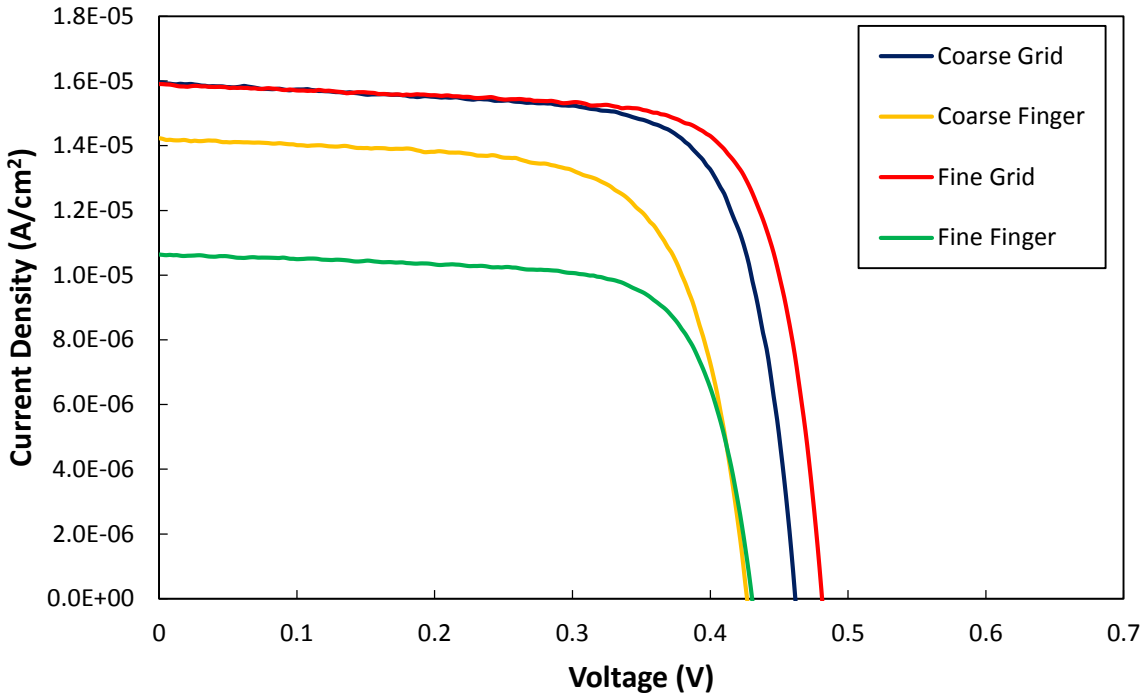

Figure 4.27 J-V curves of InGaN/GaN-Pt solar cell devices under AM 1.5 illumination

The key device metrics J_{sc} and V_{oc} for the three solar cells with Pt thicknesses of 7 nm, 10 nm and 13 nm are plotted in *Figure 4.28* and *Figure 4.29* as function of the thickness of Pt film. It is evident from *Figure 4.28* that the short-circuit current density shows a consistent overall trend independent of the device geometry and top-side electrode pitch. The short-circuit current density is maximum for all four geometries for a thickness of 10 nm of Pt. This can be explained by looking at the electrical and optical properties of the Pt films. The sheet resistance of the Pt film decreases with increase in Pt thickness which improves its ability to efficiently collect carriers. On the other hand, the optical transmission of the Pt film decreases with increase in Pt thickness which reduces the amount of light passing though it to reach the absorber layer. Since, the increase of thickness has two opposite effects on the short-circuit current density, thus, the current is maximized for an optimized

thickness of Pt which happens to be 10 nm for this case. The non-monotonic behavior is also consistent with the APSYS simulation as shown in *Figure 4.8*.

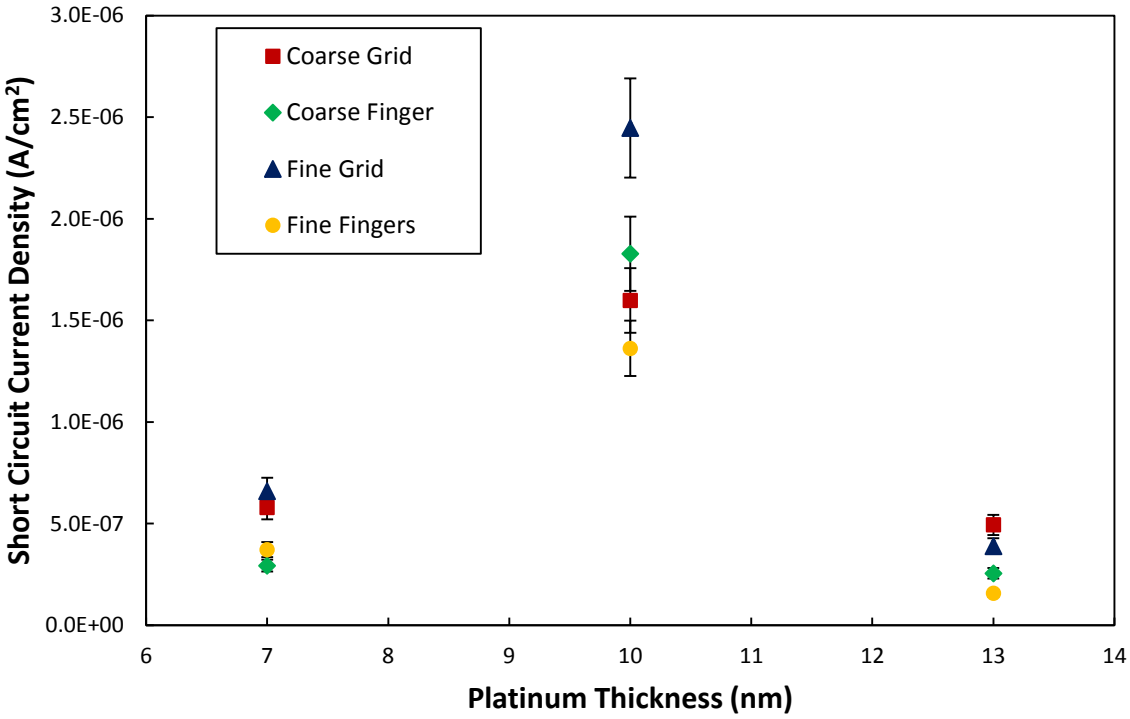

Figure 4.28 Short circuit current density as a function of Pt thickness

Figure 4.29 shows the open-circuit voltage of a solar cell as function of the thickness of Pt film used in the solar cell. No particular trend was observed between the open-circuit voltage and the Pt thickness of the film. However, the open-circuit voltage has a logarithmic dependence on the short-circuit current. Hence, small changes in short-circuit current should not affect the open-circuit voltage as seen in the APSYS simulation. As postulated before, this behavior of the open circuit voltage can be attributed to inhomogeneity of barrier heights formed across the sample; or it could be some second order effect occurring at the Pt-GaN interface. Another inference that can be drawn from the data above is that the finger geometries consistently exhibit a smaller open circuit

voltage compared to the grid geometries. This behavior is explained through a higher surface recombination probability in the finger geometries as mentioned before in the previous section, which reduces the open-circuit voltage.

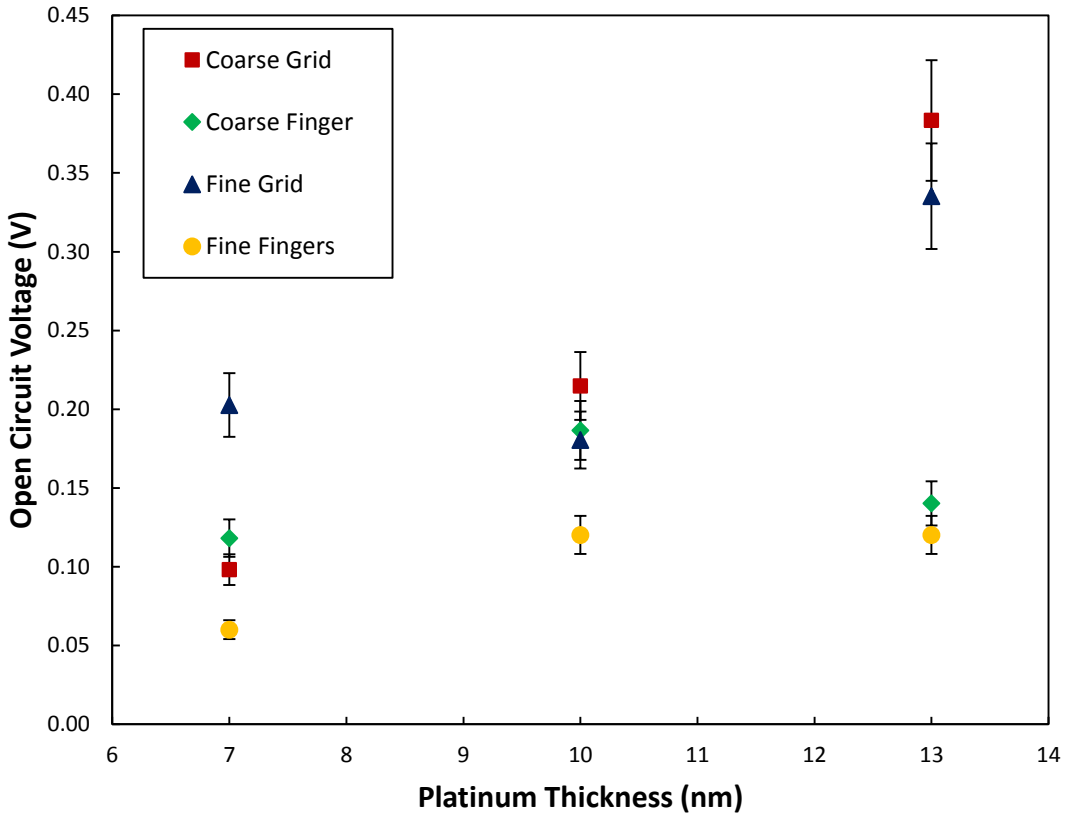

Figure 4.29 Open-circuit voltage as a function of Pt thickness

Another important observation is that these solar cells exhibit a higher short-circuit current density when illuminated by 355 nm LED source. This makes InGaN Schottky solar cells well suited for space applications where UV light is abundant. These solar cell devices were also illuminated with a 455 nm LED source which did not produce any photocurrent confirming that photons below the band gap of InGaN do not get absorbed.

We report on Pt/InGaN/GaN Schottky barrier solar cells with different thicknesses of Platinum which is being used as the transparent conductive film. Each solar cell with a different thickness of Platinum has four different electrode geometries. Relationship between solar cell performance and Pt thickness is established and explained. The impact of the contact pad geometries on the short circuit-current density and open-circuit voltage is also studied. The results show that the photovoltaic behavior of InGaN based Schottky solar cells is found to be affected by the properties of the transparent conducting layer and the contact design. Hence, it is essential to optimize transparency and conductivity of the transparent conductive layer and contact pad in order to efficiently collect photo-carriers. The present work can be an important step towards further study of InGaN based Schottky solar cells.

Chapter 5. Summary and Conclusions

Thin film solar cells made from InGaN are of considerable interest because this material system covers an unusually wide energy range (from 3.4 eV for GaN to 0.7 eV for InN), has high optical absorption coefficients, and exhibits better radiation hardness than conventional III-V semiconductors. Recently, several groups have investigated InGaN based homo-junction and hetero-junction solar cells most of which employ a p-i-n structure to enable more efficient carrier collection. However, there have been very few reports on well-conducting *p-type* InGaN with higher indium content such as would be necessary to make *p-i-n* InGaN solar cells with band gaps in the range 1.9 to 1.0 eV. The issue of p-type doping and finding a suitable p-type contact for GaN was averted in this present work by introducing a novel Schottky solar cell structure. Moreover, thin transparent conductive films made of Pt were placed in contact with *n-type* InGaN/GaN heterostructures to demonstrate the feasibility of InGaN Schottky barrier solar cells. We report on the feasibility of InGaN/GaN-Pt Schottky solar cells with different thickness of Pt (7 nm, 10 nm and 13 nm) and four different contact pad schemes. Thin films of Pt deposited on double side polished sapphire with thicknesses of 7 nm, 10 nm and 13 nm were characterized via TLM measurements and optical transmission measurements. TLM measurements showed the following results: sheet resistance of 103.9 Ω/sq., 57 Ω/sq. and 41.5 Ω/sq. for 7 nm, 10 nm and 13 nm Pt thickness films respectively. These results demonstrated that the sheet resistance decreased with increase in Pt thickness, which is expected. These results also demonstrate the ability of the electron-beam deposition system to accurately deposit thin films with at least a 3 nm accuracy. We observed a strong dependence of the transmission spectrum on the platinum thickness. The optical

transmission properties of the Pt films increased as the Pt thickness was decreased. The transmission results again confirm our ability to accurately deposit thin films. The results also show the ability of the Filmetrics measurement system to resolve transmission difference associated with thin films with such precision.

Simulations were carried out using Crosslight APYS to investigate the impact of thickness of the Pt TCO layer on the performance of GaN based solar cells. The dependence of short-circuit current and open-circuit voltage on the thickness of the Pt film was studied using simulations. Solar cell measurements were made in the dark and with LED illumination (395 nm) using a Keithley I-V sweep tool and a four-point probe measurement setup. Possible sources of error arising due to measurement setup were evaluated and were shown to cause negligible impact on the measurements. Errors arising due to variation in fabrication were addressed by eliminating devices with visible fabrication errors and the ones with high saturation current suggesting leaky behavior from the analysis. Sample variability was attributed to variation in the quality of InGaN film grown. An effort was made to address this issue, however, further investigation is required. Solar cells with 10 nm Pt as the transparent conductive film exhibited highest short circuit current density for all four types of contact pad patterns. This result is explained by optimization of the sheet resistance and transmission spectrum for the 10 nm film which enables more efficient carrier collection as compared to the solar cells with the 7 nm and 13 nm Pt films. However, no such relationship was observed between the open circuit voltage and the Pt thickness. This behavior of the open circuit voltage can be attributed to inhomogeneity of barrier heights formed across the sample; or it could be some second order effect occurring at the

Pt-GaN interface. Solar cells with the 10 nm Pt film with different contact geometries was analyzed in detail. Parameters such as surface recombination, area occupied by the opaque contact pads and series resistance are found to be responsible for affecting the short-circuit current density and open circuit voltage. Schottky barrier solar cells made with Pt exhibited higher short circuit currents when illuminated with a UV LED source (355 nm) as compared to the 395 nm LED source which confirms that Schottky barrier solar cells give better spectral response for high energy photons which are absorbed in the near depletion regions. From our study, it has been found that the optimized thickness of the Pt film for our Schottky barrier solar cell is 10 nm. This present work could be a significant step for further study of InGaN-GaN Schottky barrier solar cells.

This present work helps us in understanding the impact of the contact scheme employed in InGaN based Schottky barrier solar cells which can be utilized to improve the performance of InGaN Schottky barrier solar cells fabricated with different transparent conductive films. New materials like transparent conducting oxides need to be investigated in order to obtain contacts that offer higher transmission and lower sheet resistance. An effort has been made to optimize the grid or layer contact pad on top of the transparent conductive film. However, more optimization work still remains to be done. In summary, Pt/GaN/InGaN Schottky barrier solar cells have been investigated.

Appendix A. I-V Measurement Setup

The apparatus used to make "4-wire" I-V measurements for both TLM measurements and solar cell characterization is shown in *Figure A.1*. A Keithley 2400 SMU (Source-Measure unit) is used to source current/voltage and also probe current/voltage. The use of the SMUs has simplified device characterization that once required multiple programmable power supplies and digital multi-meters. The Model 2400's ability to source/sink up to 1A with 0.5% accuracy or better and its low noise, high impedance offers a simple cost effective alternative for PV cell characterization. The Model 2400 offers 10μV resolution on the 2V range and 100μV on the 20V range which is sufficient to accurately measure the I-V curve of any solar cell. The Model 2400's can measure low currents in the 1mA range with 10pA maximum resolution which is sufficient for virtually all dark I-V applications.

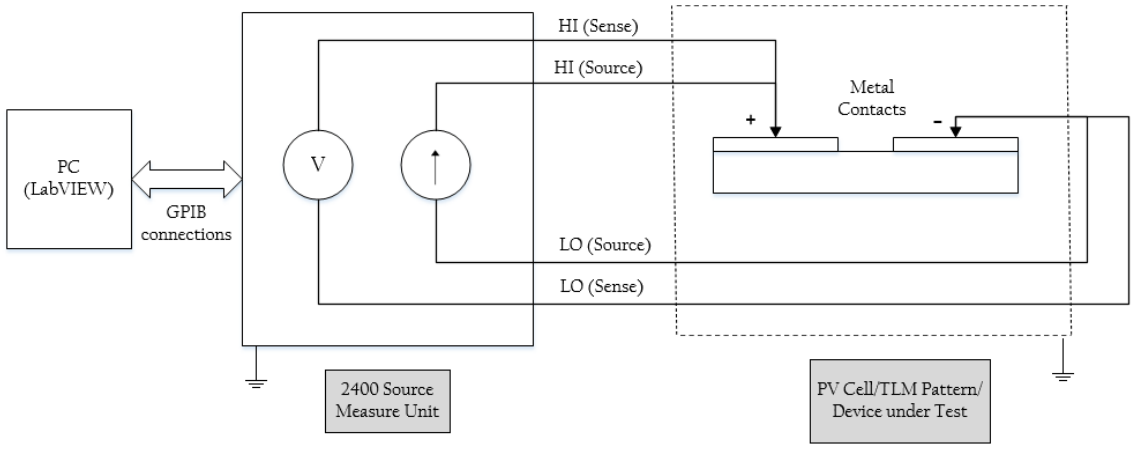

Figure A.1 I-V Measurement Apparatus Setup

A computer is used to carry out individual measurements and to collect the experimental data. A LabVIEW program is used control the Keithley 2400 source-measure meter to carry out a voltage or current sweep in specified intervals with either linear and logarithmic sweeps over the desired current or voltage ranges. The program also plots I-V

characteristics for the user to analyze. The measurements also get saved locally on the computer, which can be later on used for analysis. The Keithley 2400, although already calibrated initially by the manufacturer, was calibrated again as a part of the setup in order to determine inaccuracies in measurements due to the apparatus itself. For this, a short circuit test was conducted, which is performed by shorting out the probes in the four point measurement setup to determine the external resistances due to the probes and wires used in the setup. The value determined from this test was subtracted from actual tests to get more accurate results. All I-V measurements in this work were done using the setup described above.

REFERENCES

[1] U. S. E. I. Administration, "International Energy Outlook 2013," ed, 2013.

[2] N. O. A. Administration, "Trends in Atmospheric Carbon Dioxide," ed, 2014.

[3] M. Loster, "Total Primary Energy Supply— From Sunlight," ed, 2010.

[4] R. L. Cummerow, "Photovoltaic Effect in p-n Junctions," *Physical Review,* vol. 95, pp. 16-21, 07/01/ 1954.

[5] J. Nelson, *The Physics of Solar Cells*. UK: Imperial College Press, 2003.

[6] D. M. Chapin, C. S. Fuller, and G. L. Pearson, "A New Silicon p-n Junction Photocell for Converting Solar Radiation into Electrical Power," *Journal of Applied Physics,* vol. 25, pp. 676-677, 1954.

[7] C. Honsberg and S. Bowden. Available: http://www.pveducation.org/pvcdrom/introduction/introduction

[8] R. W. Miles, K. M. Hynes, and I. Forbes, "Photovoltaic solar cells: An overview of state-of-the-art cell development and environmental issues," *Progress in Crystal Growth and Characterization of Materials,* vol. 51, pp. 1-42, // 2005.

[9] G. Masson, M. Latour, M. Rekinger, I.-T. Theologitis, and M. Papoutsi, "Global Market Outlook for Photovoltaics 2013-2017," European Photovoltaic Industry Association.

[10] *Solar Energy Market Growth*. Available: http://www.solarbuzz.com/facts-and-figures/markets-growth/market-growth

[11] M. A. Green, *Third Generation Photovoltaics: Advanced Solar Electricity Generation,"*. Berlin: Springer-Verlag, 2003.

[12] *Best Research Cell Efficiencies*. Available: http://www.nrel.gov/ncpv/

[13] M. A. Green, K. Emery, Y. Hishikawa, W. Warta, and E. D. Dunlop, "Solar cell efficiency tables (version 43)," *Progress in Photovoltaics: Research and Applications,* vol. 22, pp. 1-9, 2014.

[14] A. Barnett, D. Kirkpatrick, C. Honsberg, D. Moore, M. Wanlass, K. Emery, *et al.*, "Milestones toward 50% efficient solar cell modules," presented at the Proc. of 22nd European PV Solar Energy Conference, Milan, Italy,.

[15] W. Shockley and H. J. Queisser, "Detailed Balance Limit of Efficiency of p-n Junction Solar Cells," *Journal of Applied Physics,* vol. 32, pp. 510-519, 1961.

[16] C. Honsberg, O. Jani, A. Doolittle, E. Trybus, G. Namkoong, I. Ferguson, *et al.*, "InGaN – A New Solar Cell Material," in *Proceedings of the 19th European Photovoltaic Science and Engineering Conference*, Paris, France, pp. 15-20.

[17] O. K. Jani, "Development of wide-band gap InGaN solar cells for high efficiency photovoltaics," Ph.D. dissertation, Electrical and Computer Engineering Department, Georgia Institute of Technology, 2008.

[18] J. Wu and W. Walukiewicz, "Band gaps of InN and group III nitride alloys," *Superlattices and Microstructures,* vol. 34, pp. 63-75, 7// 2003.

[19] J. Wu, W. Walukiewicz, K. M. Yu, J. W. Ager, E. E. Haller, H. Lu, *et al.*, "Small band gap bowing in In[sub 1−x]Ga[sub x]N alloys," *Applied Physics Letters,* vol. 80, p. 4741, 2002.

[20] J. Wu, W. Walukiewicz, K. M. Yu, W. Shan, J. W. Ager, E. E. Haller, *et al.*, "Superior radiation resistance of In[sub 1−x]Ga[sub x]N alloys: Full-solar-spectrum photovoltaic material system," *Journal of Applied Physics,* vol. 94, p. 6477, 2003.

[21] S. Nakamura, T. Mukai, and M. Senoh, "Candela-class high-brightness InGaN/AlGaN double-heterostructure blue-light-emitting diodes," *Applied Physics Letters,* vol. 64, pp. 1687-1689, 1994.

[22] S. Nakamura, M. Senoh, N. Iwasa, and S.-i. Nagahama, "High-Brightness InGaN Blue, Green and Yellow Light-Emitting Diodes with Quantum Well Structures," *Jpn. J. Appl. Phys.*, vol. 34, pp. L 797-L 799, 1995.

[23] S. Nakamura, M. Senoh, S.-i. Nagahama, N. Iwasa, T. Yamada, T. Matsushita, *et al.*, "Room-temperature continuous-wave operation of InGaN multi-quantum-well-structure laser diodes with a long lifetime," *Applied Physics Letters,* vol. 70, pp. 868-870, 1997.

[24] W. Yong, Z. Yonggang, M. Xiaohui, Y. Naisen, D. Dongmei, and L. Kei May, "Progress on the GaN-based LEDs and LDs," in *Optoelectronics and Microelectronics (ICOM), 2012 International Conference on*, 2012, pp. 105-110.

[25] E. Trybus, O. Jani, S. Burnham, I. Ferguson, C. Honsberg, M. Steiner, *et al.*, "Characteristics of InGaN designed for photovoltaic applications," *physica status solidi (c),* vol. 5, pp. 1843-1845, 2008.

[26] X. Zheng, R.-H. Horng, D.-S. Wuu, M.-T. Chu, W.-Y. Liao, M.-H. Wu, *et al.*, "High-quality InGaN/GaN heterojunctions and their photovoltaic effects," *Applied Physics Letters*, vol. 93, p. 261108, 2008.

[27] M. Anani, H. Abid, Z. Chama, C. Mathieu, A. Sayede, and B. Khelifa, "InxGa1−xN refractive index calculations," *Microelectronics Journal*, vol. 38, pp. 262-266, 2// 2007.

[28] J. Wu, "When group-III nitrides go infrared: New properties and perspectives," *Journal of Applied Physics*, vol. 106, pp. -, 2009.

[29] O. Jani, I. Ferguson, C. Honsberg, and S. Kurtz, "Design and characterization of GaN/InGaN solar cells," *Applied Physics Letters*, vol. 91, p. 132117, 2007.

[30] F. Bernardini and V. Fiorentini, "Spontaneous versus Piezoelectric Polarization in III–V Nitrides: Conceptual Aspects and Practical Consequences," *physica status solidi (b)*, vol. 216, pp. 391-398, 1999.

[31] F. Bernardini and V. Fiorentini, "Nonlinear macroscopic polarization in III-V nitride alloys," *Physical Review B*, vol. 64, p. 085207, 08/08/ 2001.

[32] S. Nakamura and T. Mukai, "High Quality InGaN Films grown on GaN Films," *Jpn. J. Appl. Phys.*, vol. 31, pp. L 1457-L 1459, 1992.

[33] X.-m. Cai, S.-w. Zeng, and B.-p. Zhang, "Fabrication and characterization of InGaN p-i-n homojunction solar cell," *Applied Physics Letters*, vol. 95, p. 173504, 2009.

[34] X. Chen, K. D. Matthews, D. Hao, W. J. Schaff, and L. F. Eastman, "Growth, fabrication, and characterization of InGaN solar cells," *physica status solidi (a)*, vol. 205, pp. 1103-1105, 2008.

[35] C. J. Neufeld, N. G. Toledo, S. C. Cruz, M. Iza, S. P. DenBaars, and U. K. Mishra, "High quantum efficiency InGaN/GaN solar cells with 2.95 eV band gap," *Applied Physics Letters*, vol. 93, p. 143502, 2008.

[36] E. Matioli, C. Neufeld, M. Iza, S. C. Cruz, A. A. Al-Heji, X. Chen, *et al.*, "High internal and external quantum efficiency InGaN/GaN solar cells," *Applied Physics Letters*, vol. 98, p. 021102, 2011.

[37] J. R. Lang, C. J. Neufeld, C. A. Hurni, S. C. Cruz, E. Matioli, U. K. Mishra, *et al.*, "High external quantum efficiency and fill-factor InGaN/GaN heterojunction

solar cells grown by NH[sub 3]-based molecular beam epitaxy," *Applied Physics Letters,* vol. 98, p. 131115, 2011.

[38] C. J. Neufeld, C. Zhen, S. C. Cruz, N. G. Toledo, S. P. DenBaars, and U. K. Mishra, "Optimization of the p-GaN window layer for InGaN/GaN solar cells," in *Photovoltaic Specialists Conference (PVSC), 2010 35th IEEE*, 2010, pp. 002089-002092.

[39] O. Jani, C. Honsberg, Y. Huang, J. O. Song, I. Ferguson, G. Namkoong, *et al.*, "Design, Growth, Fabrication and Characterization of High-Band Gap InGaN/GaN Solar Cells," in *Photovoltaic Energy Conversion, Conference Record of the 2006 IEEE 4th World Conference on*, 2006, pp. 20-25.

[40] O. Jani, B. Jampana, M. Mehta, H. Yu, I. Ferguson, R. Opila, *et al.*, "Optimization of GaN window layer for InGaN solar cells using polarization effect," in *Photovoltaic Specialists Conference, 2008. PVSC '08. 33rd IEEE*, 2008, pp. 1-4.

[41] O. Jani, C. Honsberg, A. Asghar, D. Nicol, I. Ferguson, A. Doolittle, *et al.*, "Characterization and analysis of InGaN photovoltaic devices," in *Photovoltaic Specialists Conference, 2005. Conference Record of the Thirty-first IEEE*, 2005, pp. 37-42.

[42] H. Ray-Hua, L. Shih-Ting, T. Yu-Li, C. Mu-Tao, L. Wen-Yih, W. Ming-Hsien, *et al.*, "Improved Conversion Efficiency of GaN/InGaN Thin-Film Solar Cells," *Electron Device Letters, IEEE*, vol. 30, pp. 724-726, 2009.

[43] L. Hsu and W. Walukiewicz, "Modeling of InGaN/Si tandem solar cells," *Journal of Applied Physics,* vol. 104, p. 024507, 2008.

[44] A. R. Lothar, G. Iulian, Y. Kin Man, M. K. Vincent, W. Wladek, and W. A. Joel, III, "Demonstration of a III–Nitride/Silicon Tandem Solar Cell," *Applied Physics Express,* vol. 2, p. 122202, 2009.

[45] R. Dahal, B. Pantha, J. Li, J. Y. Lin, and H. X. Jiang, "InGaN/GaN multiple quantum well solar cells with long operating wavelengths," *Applied Physics Letters,* vol. 94, p. 063505, 2009.

[46] R. Dahal, J. Li, K. Aryal, J. Y. Lin, and H. X. Jiang, "InGaN/GaN multiple quantum well concentrator solar cells," *Applied Physics Letters,* vol. 97, p. 073115, 2010.

[47] S. Jinn-Kong, Y. Chih-Ciao, T. Shang-Ju, C. Kuo-Hua, L. Ming-Lun, W.-C. Lai, *et al.*, "Demonstration of GaN-Based Solar Cells With GaN/InGaN Superlattice Absorption Layers," *Electron Device Letters, IEEE,* vol. 30, pp. 225-227, 2009.

[48] A. Bhuiyan, K. Sugita, A. Hashimoto, and A. Yamamoto, "InGaN Solar Cells: Present State of the Art and Important Challenges," *Photovoltaics, IEEE Journal of,* vol. 2, pp. 276-293, 2012.

[49] J. Xue, D. Chen, B. Liu, Z. Xie, R. Jiang, R. Zhang, *et al.*, "Au/Pt/InGaN/GaN Heterostructure Schottky Prototype Solar Cell," *Chin. Phys. Lett.*, vol. 26, 2009.

[50] S. Lin, B. P. Zhang, S. W. Zeng, X. M. Cai, J. Y. Zhang, S. X. Wu, *et al.*, "Preparation and properties of Ni/InGaN/GaN Schottky barrier photovoltaic cells," *Solid-State Electronics,* vol. 63, pp. 105-109, 9// 2011.

[51] C. Wang and R. F. Davis, "Deposition of highly resistive, undoped, and p-type, magnesium-doped gallium nitride films by modified gas source molecular beam epitaxy," *Applied Physics Letters,* vol. 63, pp. 990-992, 1993.

[52] X. Guo and E. F. Schubert, "Current crowding in GaN/InGaN light emitting diodes on insulating substrates," *Journal of Applied Physics,* vol. 90, p. 4191, 2001.

[53] X. Zheng, L. Tang, D. Zhang, J. Dong, and H. Yang, "Effect of contact spreading layer on photovoltaic response of InGaN-based solar cells," *physica status solidi (a),* vol. 208, pp. 199-201, 2011.

[54] X. M. Cai, Y. Wang, Z. D. Li, X. Q. Lv, J. Y. Zhang, L. Y. Ying, *et al.*, "Improved photovoltaic performance of InGaN/GaN solar cells with optimized transparent current spreading layers," *Applied Physics A,* vol. 111, pp. 483-486, 2013.

[55] J.-P. Shim, J. Seong-Ran, J. Yon-Kil, and D.-S. Lee, "Improved Efficiency by Using Transparent Contact Layers in InGaN-Based p-i-n Solar Cells," *Electron Device Letters, IEEE,* vol. 31, pp. 1140-1142, 2010.

[56] E. H. Rhoderick, *Metal-Semiconductor Contacts*: Oxford University Press, 1978.

[57] Q. Z. Liu and S. S. Lau, "A review of the metal–GaN contact technology," *Solid-State Electronics,* vol. 42, pp. 677-691, 5/6/ 1998.

[58] J.-K. Ho, C.-S. Jong, C. C. Chiu, C.-N. Huang, C.-Y. Chen, and K.-K. Shih, "Low-resistance ohmic contacts to p-type GaN," *Applied Physics Letters,* vol. 74, p. 1275, 1999.

[59] J.-K. Ho, C.-S. Jong, C. C. Chiu, C.-N. Huang, K.-K. Shih, L.-C. Chen, *et al.*, "Low-resistance ohmic contacts to p-type GaN achieved by the oxidation of Ni/Au films," *Journal of Applied Physics,* vol. 86, p. 4491, 1999.

[60] J. M. Essick and R. T. Mather, "Characterization of a bulk semiconductor's band gap via a near-absorption edge optical transmission experiment," *American Journal of Physics,* vol. 61, pp. 646-649, 1993.

[61] K. M. Yu, M. A. Mayer, D. T. Speaks, H. He, R. Zhao, L. Hsu, *et al.*, "Ideal transparent conductors for full spectrum photovoltaics," *Journal of Applied Physics,* vol. 111, pp. -, 2012.

[62] T. Koida, H. Sai, H. Shibata, and M. Kondo, "Trend of transparent conductive oxides for solar cells," in *Active-Matrix Flatpanel Displays and Devices (AM-FPD), 2012 19th International Workshop on*, 2012, pp. 45-48.

[63] D. S. Ginley and C. Bright, "Transparent Conducting Oxides," *MRS Bulletin,* vol. 25, pp. 15-18, 2000.

[64] D. S. Ginley and J. D. Perkins, *Handbook of Transparent Conductors*. New York: Springer Science+Business, 2010.

[65] G. K. Reeves and H. B. Harrison, "Obtaining the specific contact resistance from transmission line model measurements," *Electron Device Letters, IEEE,* vol. 3, pp. 111-113, 1982.